

Diagnostic Tests of Models for the Thermal Structure of the Non-Precipitating Convective Boundary Layer

By
Douglas A. Moore and Alan K. Betts

Department of Atmospheric Science
Colorado State University
Fort Collins, Colorado

This research was supported by the National Science Foundation, Atmospheric Sciences Section under Grants GA-33182 and GA-36323.

Principal investigator: A.K. Betts

April 1974



**Department of
Atmospheric Science**

Paper No. 217

DIAGNOSTIC TESTS OF MODELS FOR THE THERMAL STRUCTURE
OF THE NON-PRECIPITATING CONVECTIVE BOUNDARY LAYER

by

Douglas A. Moore

and

Alan K. Betts

This research was supported by the National Science Foundation,
Atmospheric Sciences Section under Grants GA-33182 and GA-36323,

Principal Investigator: A. K. Betts

Department of Atmospheric Science

Colorado State University

Fort Collins, Colorado

80521

April 1974

Atmospheric Science Paper Number 217

ABSTRACT

DIAGNOSTIC TESTS OF MODELS FOR THE THERMAL STRUCTURE OF THE NON-PRECIPITATING CONVECTIVE BOUNDARY LAYER

This paper presents a diagnostic study of two models proposed by Betts (1973a). The first was a model for a well mixed sub-cloud layer capped by a more stable transition layer (see Fig. 2.1). The downward heat flux at the base of this transition layer is here estimated from the thermal structure of the layer to be 15-25% of the surface sensible heat flux.

The second model was a model for a two layer lapse-rate structure for the cumulus layer. A sensitivity analysis is conducted on this lapse-rate model. The model results compare favorably with observational evidence from the BOMEX, ATEX and VIMHEX tropical field experiments. The parameterization of entrainment is examined through model calculations, and by radiosonde ascents into cloud. It is found that the scaling of entrainment by the depth of the layer of conditional instability (as used in the model) is satisfactory; but that other depths of the cloud layer could be used equally well.

ACKNOWLEDGEMENTS

This research was supported by the Atmospheric Sciences Section of the National Science Foundation under Grants GA-33182 and GA-36323. The VIMHEX II field experiment was additionally supported by the Office of Naval Research under Contract Number N00 014-68A-0493-002, the Facilities Laboratory of the National Centre for Atmospheric Research, and the Meteorological Service of the Venezuelan Air Force.

Douglas A. Moore wishes to thank the United States Air Force for the school assignment which enabled him to carry out this research.

We also acknowledge the assistance of Ms. P. Martin, Ms. S. Kuehl and Mr. R. Miller in drafting, typing and computer programming.

TITLE: DIAGNOSTIC TESTS OF MODELS FOR THE THERMAL STRUCTURE OF
THE NON PRECIPITATING CONVECTIVE BOUNDARY LAYER

TABLE OF CONTENTS

	<u>PAGE</u>
ABSTRACT	iii
ACKNOWLEDGEMENTS	iv
TABLE OF CONTENTS	v
LIST OF TABLES	vii
LIST OF FIGURES	viii
SYMBOL LIST	xi
SUBSCRIPTS	xiii
1. INTRODUCTION	1
1.1 General Discussion	1
1.2 Objectives of This Paper	1
2. DATA	3
2.1 Sources of Data	3
2.2 Thermodynamic Variables	6
3. SUB-CLOUD LAYER	7
3.1 Description	7
3.2 Entrainment Induced Downward Heat Flux	9
4. CUMULUS LAYER	13
4.1 Description	13
4.2 Lapse-Rate Model	15
4.3 Numerical Solutions of Lapse-Rate Model	18
4.4 Sensitivity Tests of Lapse-Rate Model	24
4.5 Model Comparisons with Observational Data	25

TABLE OF CONTENTS - Continued

	<u>Page</u>
4.6 Determination of Dilution Scale Length From In-Cloud Radiosonde Ascents	44
4.7 Parameterization of Entrainment	46
5. SUMMARY AND CONCLUSIONS	52
REFERENCES	53
APPENDIX A	55
APPENDIX B	59

LIST OF TABLES

<u>TABLE</u>		<u>PAGE</u>
3.1	Calculated values of k from selected sondes scaled by transition layer base.	12
4.1	Sensitivity analysis of lapse-rate model parameters.	24
4.2	Input values for lapse-rate model calculations.	26
4.3	Average of soundings 1300-1500 local standard time during suppressed convection.	27
4.4	Comparison of model results to observed values.	29
4.5	Model calculations for $E = .45$, $D = .60$	40
4.6	Dilution scale length as deduced from in-cloud radiosonde ascents.	45

LIST OF FIGURES

	<u>PAGE</u>
Figure 2.1 - Sketch of the six levels used by Augstein et al (1973) to describe the structure of the thermal boundary layer below the trade inversion.	4
Figure 3.1a - Thermal structure, parcel path, and heat flux in the dry convective layer from Betts (1973a).	8
Figure 3.1b - Model structure and heat flux for a dry convective layer from Betts (1973a).	8
Figure 3.2 - Average of selected sondes scaled by observed transition layer base, TL#1.	10
Figure 3.3 - Average of selected sondes scaled by observed transition layer base, TL#2.	11
Figure 4.1 - Sketch tephigram through cumulus layer depicting typical parcel paths ($\theta_e(p)$, $\theta_{es}(p)$ and $\theta(p)$, $\theta_L(p)$) for a cloud parcel diluting with its environment. θ_e and θ_{es} values are read off the wet adiabats while θ_L and θ values are read off the dry adiabats, from Betts (1973a).	14
Figure 4.2a - Lapse-rate model for the cumulus layer from Betts (1973a). Heat flux profile is purely schematic.	16
Figure 4.2b - Two-layer model stratification with cloud parcel path on ascent. Shaded region represents the maximum available positive potential energy from Betts (1973a).	16
Figure 4.3 - Model calculations of $\Gamma_1 = f(\bar{\Gamma})$ for various cloud parcel lapse-rates (Γ_c) and mean stratification ($\bar{\Gamma}$) for $E = .45$, $D = .60$	20
Figure 4.4 - Model calculations of $\Gamma_2 = f(\bar{\Gamma})$ for various cloud parcel lapse-rates (Γ_c) and mean stratification ($\bar{\Gamma}$) for $E = .45$, $D = .60$	21
Figure 4.5 - Model calculations of $\Delta Z_1/\Delta Z_2 = f(\bar{\Gamma})$ for various cloud parcel lapse-rates (Γ_c) and mean stratification ($\bar{\Gamma}$) for $E = .45$, $D = .60$	22
Figure 4.6 - Model calculations of $\Gamma_1/\Gamma_2 = f(\bar{\Gamma})$ for various cloud parcel lapse-rates (Γ_c) and mean stratification ($\bar{\Gamma}$) for $E = .45$, $D = .60$	23

LIST OF FIGURES - Continued

	<u>PAGE</u>
Figure 4.7 - BOMEX sounding with lapse-rate model solution superimposed (Holland and Rasmusson, 1973). Dots are data points, straight lines are lapse rates predicted by the model.	30
Figure 4.8 - ATEX sounding with lapse-rate model solution superimposed (Augstein et al, 1973). Dots are data levels (see section 2.1 and Fig. 2.1).	31
Figure 4.9 - Time averaged VIMHEX II sondes with lapse-rate model solution superimposed.	32
Figure 4.10 - VIMHEX II sondes 39, 42, 53, 65 with lapse-rate model solution superimposed.	33
Figure 4.11 - VIMHEX II sondes 105, 108, 111, 113 with lapse-rate model solution superimposed.	34
Figure 4.12 - VIMHEX II sondes 146, 201, 211, 230 with lapse-rate model solution superimposed.	35
Figure 4.13 - VIMHEX II sondes 253, 260, 302, 328 with lapse-rate model solution superimposed.	36
Figure 4.14 - Histogram of $\bar{\Gamma} - \Gamma_c$ for all cases tested.	37
Figure 4.15 - Observed Γ_1/Γ_2 ratios for land and oceanic cases.	38
Figure 4.16 - Relative errors of lapse-rates (Γ_1, Γ_2) for the "best fit" model results and for the model results for $E = .45, E = .60$	41
Figure 4.17 - Histogram of values for E and E + D.	42
Figure 4.18 - Vertical speed shear of VIMHEX II sondes 65 and 230.	43
Figure 4.19 - Regression analysis of the dilution scale length (S) onto the observed value of ΔZ_1 . Correlation coefficient of .76. Dashed line indicates $E = .42$	47
Figure 4.20 - Regression analysis of S onto Z_1 . Correlation coefficient of .76.	48
Figure 4.21 - Regression analysis of S onto ΔZ . Correlation coefficient of .86. Dashed line ($S = 1.2 \Delta Z$) corresponds to $\Delta Z/a = 6.5$ from Betts (1973b).	49

LIST OF FIGURES - Continued

	<u>PAGE</u>
Figure 4.22 - Regression analysis of S onto Z_2 . Correlation coefficient of .86.	50

LIST OF SYMBOLS

T	temperature
θ	potential temperature
θ_v	virtual potential temperature
θ_e	equivalent potential temperature
θ_{es}	saturation equivalent potential temperature
θ_L	liquid water potential temperature
F_θ	flux of $\rho C_p \theta$: potential heat flux
F_{θ_L}	flux of $\rho C_p \theta_L$: total heat flux
Γ	$\partial\theta/\partial z$
Γ_w	$\partial\theta/\partial z$ for wet adiabat
Γ_c	$\partial\theta/\partial z$ for cloud parcel
LCL	lifting condensation level
p	pressure
\hat{p}	scaled pressure: BOMEX
p^*	scaled pressure: section 3.2
r	water vapor mixing ratio
r_s	saturation water vapor mixing ratio
r_L	liquid water mixing ratio
q_s	$r_s/(1+r)$
q_L	$r_L/(1+r)$
C_p	specific heat of air at constant pressure
L	latent heat of vaporization of water
R_v	gas constant for 1 gram of water vapor
R	$\frac{L}{C_p T}(r_s(e) - r(e))$ a measure of the unsaturation of the environment

LIST OF SYMBOLS - Continued

J	ratio of saturation specific heat of air to the dry specific heat at constant pressure (C_p)
$\Delta\theta$	inversion strength: Figure 3.1b
ρ	air density
S	scale length for dilution
E	dilution or entrainment parameter
D	kinetic energy dissipation parameter: section 4.3
M	mass of parcel
W	vertical air velocity
a	cloud radius
K_2	entrainment constant: section 4.7
Z	height coordinate
t	time
k	heat flux proportionality constant: section 3.1
\sim	horizontal average
—	vertical average
'	deviation from mean
(e)	environmental property
(p)	parcel property
(c)	cloud parcel property

SUBSCRIPTS

m	mixed layer property at level m of sub-cloud layer
o	surface property
b	cloud base variable
$\binom{1}{2}$	variables at levels $\binom{1}{2}$ of cumulus layer
d	dry layer property
R	radiation variable

1. INTRODUCTION

1.1 General Discussion

The tropics provide a large amount of the sensible and latent heat required to drive the general circulation. It has long been recognized that to effectively forecast global weather, significant strides must be made in the modelling of the tropical atmosphere, whose structure is strongly conditioned by cumulus convection organized on a variety of scales. It is to this end that a series of tropical field experiments, such as BOMEX, ATEX, VIMHEX and, this summer, GATE, have been organized. It is unlikely to be possible, even from satellites, to observe convective motions in sufficient detail to predict their development, unless we have a better understanding of the physical processes and feedback between convection on all scales and the synoptic-scale. With a better understanding it is hoped to be able to parameterize the net effects of cumulus convection in terms of a larger "grid-scale" of perhaps 200 km, by relating the subgrid-scale processes to the larger-scale parameters.

There have been many approaches to this parameterization problem. Convective adjustment has been used in general circulation models (Manabe et al, 1966), while Kuo (1965) suggested a simple detraining cloud model. Ooyama (1964) and Charney and Eliason (1964) coupled convection to boundary layer convergence, and more recently Arakawa and Schubert (1974) have proposed a parameterization theory based on a cumulus ensemble model. We know that the atmosphere usually achieves some balanced structure: a balance between large-scale forcing and the convective sources and transports (see, for example, Betts, 1974b).

1.2 Objectives of This Paper

This paper is concerned with models for the structure of the non-precipitating convective boundary layer; that is with shallow cumulus development (such as the tradewind boundary layer) where precipitation can, as a first approximation, be neglected. Diagnostic studies such as Holland and Rasmusson (1973) have shown that the tradewind convective layer is a balanced state, in which the Trade inversion is maintained by a downward heat transport and upward vapor transport by cumulus clouds against the subsiding large-scale motion. This was predicted theoretically by Betts (1970, 1973a). In these papers, Betts proposed a model for the mixed subcloud layer and a lapse-rate model to represent the balanced thermal structure in the cumulus layer. Together these models formed the basis for a parameterization theory based on convective adjustment for a shallow cumulus layer.

The main purpose of this paper (Chapter 4) is a diagnostic study of the one dimensional lapse-rate model of Betts (1970, 1973a) to see whether the model, used diagnostically, predicts the balanced structure observed. The model will be solved for a large range of tropical values, and tested against observational data from VIMHEX II, BOMEX, and ATEX experiments; thus yielding evaluations of the model for oceanic and land based convection. A further objective is to provide some insight into the parameterization of entrainment into cumulus clouds. The fractional rate of dilution $\frac{1}{M} \frac{dM}{dz}$, of cloud mass will be represented by a dilution scale length (S). The dilution scale length will be related to various depths of the cumulus layer.

In Chapter 3 a brief study will be made of one aspect of the mixed subcloud layer model, namely the shallow inversion usually observed at cloud-base (called the "transition layer") and the heat flux into the subcloud layer at the base of this inversion.

2. DATA

2.1 Sources of Data

Data were obtained from BOMEX, ATEX and VIMHEX II.

The BOMEX data were from a five-day undisturbed period, June 22-26, 1969 (Holland and Rasmusson, 1973). Radiosondes were launched at $1\frac{1}{2}$ hour intervals. The original data were analyzed at each level with any values greater than three standard deviations from the mean discarded. The data were filtered to remove frequencies of periodicity less than six hours. The diurnal variation of humidity was removed to minimize the radiosonde hygrometer errors.

The ATEX data used were obtained (Augstein, et al, 1973) from sondes launched from the F. S. Meteor and W. F. S. Planet during the period 7 February - 20 February 1969. The ships' locations varied from 5.8 N to 14.0 N and from 34.5 W to 38.4 W. Data obtained from each sonde were analyzed and the following levels were determined by Augstein, et al. (See Fig. 2.1).

Z_m	top of the mixed layer,
Z_t	top of the transition layer,
Z_{ib}	base of the inversion,
Z_{it}	top of the inversion,
Z_{icb}	base of the inversion core
Z_{ict}	top of the inversion core.

That is, each sounding was divided below the top of the trade inversion into six layers, so as to preserve these six layers when averages were generated (See Augstein, et al). The data used here are average profiles each containing from twelve to twenty-four sondes.

VIMHEX II, designed to study the structure of the tropical atmosphere over land, was carried out during the summer of 1972 at Carrizal, Venezuela.

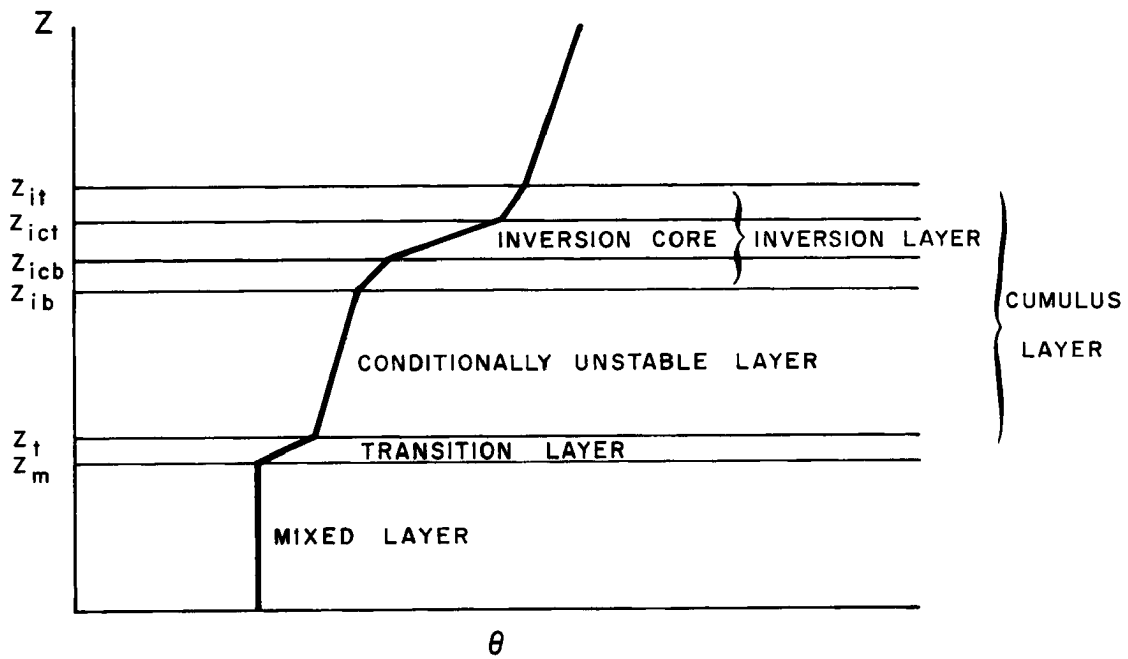


Figure 2.1 - Sketch of the six levels used by Augstein et al (1973) to describe the structure of the thermal boundary layer below the trade inversion.

Three hundred and twenty seven radiosondes were launched to study the convective atmosphere during a period from May to early September 1972. Additional information was available from the synoptic radiosonde and pibal network, surface observations, a mesoscale rainfall network, a 10 cm radar and some research aircraft flights. This study is based on radiosonde data from days without precipitation, or before the onset of precipitation. The radiosonde data were reduced at two levels of vertical resolution: "one minute" data which has a 20-25 mb resolution at low levels, and "contact level" data which has a resolution of about 10 mb in the low levels (VIZ 1290 series radiosonde). A paper by Dugan (1973) discusses the structure of the subcloud layer based on these data. He found, for example, that the height of cloud-base could be estimated closely from the lifting condensation level of air just above the superadiabatic layer. This was checked by timing a limited number of radiosondes which rose through the base of a cloud, so as to determine the actual cloud-base height from the radiosonde strip chart. Another conclusion relevant to this study (see also Betts et al, 1974), was that except near saturation (>90%) the daytime humidity measurements by the new VIZ 1290 series sonde were within 2% of their true values.

Two averaging techniques were used on some VIMHEX II data in this study. A few time averaged samples are used (e.g. of sondes between 1300 and 1500 local time - see Table 4.5) although this technique tends to obscure the finer details of the atmospheric structure, when the convective layer is at different stages of development. In the study of the subcloud layer (section 3.2) averages were generated in a p^* coordinate system with $p^* = 0$ and $p^* = 1$ corresponding respectively to the surface and the base of the transition layer, which was chosen as the level where the potential temperature increased sharply from its nearly constant value in the subcloud layer (see pp. 9).

2.2 Thermodynamic Variables

Data obtained from radiosonde measurements include temperature and relative humidity vertical profiles. The vertical temperature profile has a one to one functional relationship with potential temperature (θ) and a saturation equivalent potential temperature (θ_{es}). With the addition of the moisture profile, the equivalent potential temperature (θ_e) is uniquely determined.

In the study of non-precipitating cumulus convection, it is convenient to use the liquid water potential temperature, θ_L . θ_L is the temperature a parcel would have if all its liquid water were to be evaporated through wet adiabatic descent (Betts, 1970, 1973a). The variable pair (θ_{es} , θ_L) will be used in this study of cumulus convection.

Their approximate definitions are:

$$\theta_{es} \approx \theta \exp \left(\frac{Lq_s}{C_p T} \right) \quad (2.1)$$

and

$$\theta_L \approx \theta \exp \left(- \frac{Lq_L}{C_p T} \right) \quad (2.2)$$

If $q_L = 0$, then $\theta_L = \theta$, and if the parcel is saturated, $\theta_{es} = \theta_e$.

3. SUB-CLOUD LAYER

3.1 Description of Model

This chapter is a brief study of a model for the thermal structure of the subcloud layer. Figure 3.1a shows a sketch of the structure typically observed. The absorption of short wave solar energy produces a superadiabatic layer near the surface, and sensible and latent heat fluxes to the atmosphere. Parcels rising from this layer dilute with the lower θ environmental air; consequently, following a path as depicted in Fig. 3.1a. The parcel constantly loses kinetic energy through turbulent diffusion and dilution. In general, the parcel will overshoot the level where $\theta(p) = \theta(e)$ because of positive kinetic energy. This overshoot cools the environment since $\theta(p) < \theta(e)$, producing a downward heat flux at the top of the layer. The parcel stops rising when all its kinetic energy is expended, and then will fall back with a damped oscillation about some level in the transition layer (the more stable layer shown). This overshoot process, which is damped because of mixing and dissipation of kinetic energy incorporates or entrains air from above the stable layer into the nearly well mixed layer. That is, the inversion is pushed upwards by the cooling effect of the negatively buoyant parcels, represented in Fig. 3.1a by a downward heat flux at Z_m . This process is discussed in more detail in Betts (1970) and Stull (1973).

Betts (1973a) has proposed a model of the sub-cloud layer where the transition layer (Fig. 3.1a) is replaced by a sharp inversion (Fig. 3.1b). There is a corresponding heat flux jump at Z_m . Further this entrainment induced downward heat flux at Z_m ($F_{m\theta}$) was assumed proportional to the surface heat flux ($F_{0\theta}$) where:

$$F_{m\theta} = -kF_{0\theta} \quad (3.1)$$

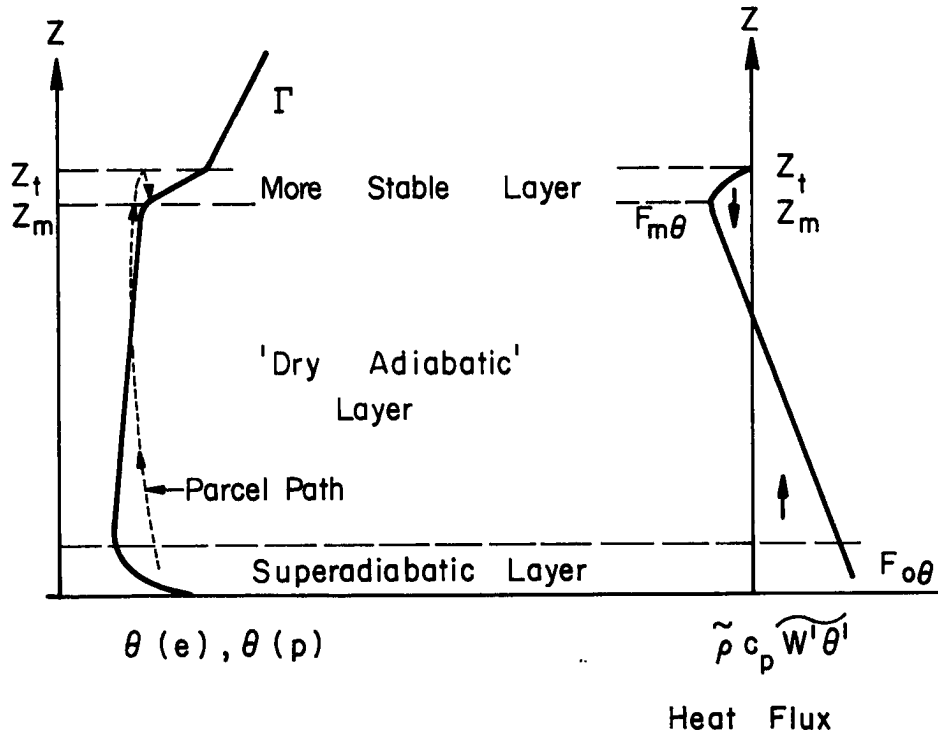


Figure 3.1a - Thermal structure, parcel path, and heat flux in the dry convective layer from Betts (1973a).

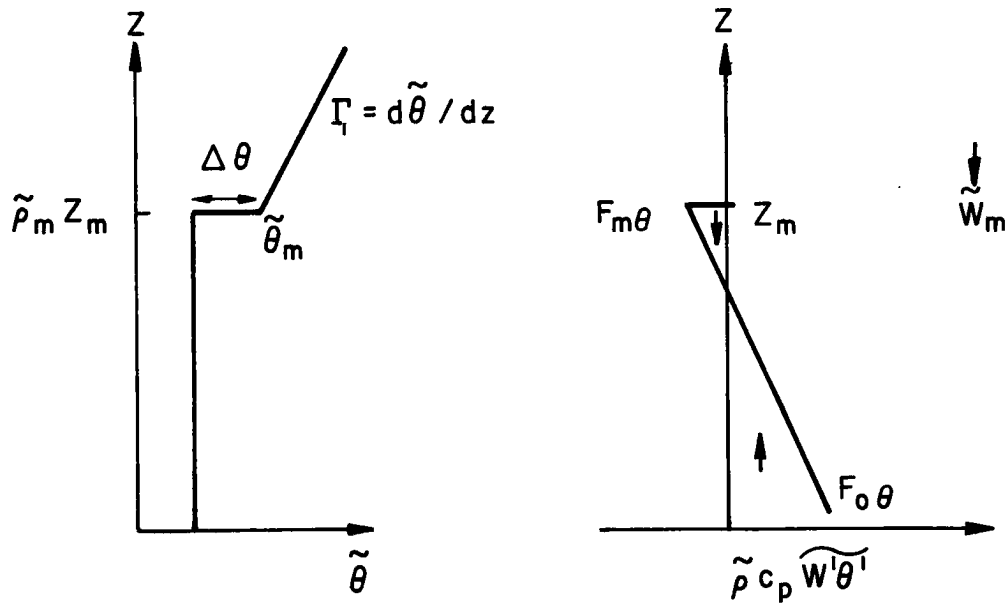


Figure 3.1b - Model structure and heat flux for a dry convective layer from Betts (1973a).

Ball (1960) showed that if $k = 1$, there is no dissipation of kinetic energy. Tennekes (1973) and Carson (1973) have suggested values for k of .2 and .5, respectively. The inversion strength (Fig. 3.1b), $\Delta\theta$, is related to k by (see Appendix A for model equations of Betts 1973a):

$$\Delta\theta \approx \frac{k \Gamma_1 Z_m}{k + 1} \quad (3.2)$$

where the variation of density with height has been neglected. The inversion strength is observable from selected radiosonde ascents with a well-defined transition layer, and $\Delta\theta$ will be used to determine an approximate value for k to incorporate in dry convective models.

3.2 Entrainment Induced Downward Heat Flux

Twenty-five VIMHEX II soundings were selected which exhibited a well-defined transition layer (that is a sharp stable layer near cloud base, taken as the L. C. L.) between 890 and 920 mb. The sondes were divided into two samples (TL1 and TL2). The thirteen sondes with the lowest transition base height, and the twelve with the highest comprised TL1 and TL2, respectively. These sondes were scaled with respect to their transition layer base:

$$p^* = \frac{p_{\text{surface}} - p(I)}{p_{\text{surface}} - p_{\text{transition base}}}$$

when

$$\begin{aligned} p(I) &= p_{\text{surface}} & p^* &= 0 \\ p(I) &= p_{\text{transition base}} & p^* &= 1.0 \end{aligned}$$

The top of the surface layer corresponds approximately to $p^* = .20$. Averages of the TL1 and TL2 sondes were computed from the scaled sondes, after which, the average pressure and height values were reinstated. Figures 3.2 and 3.3 depict the θ and θ_v profiles for the two average

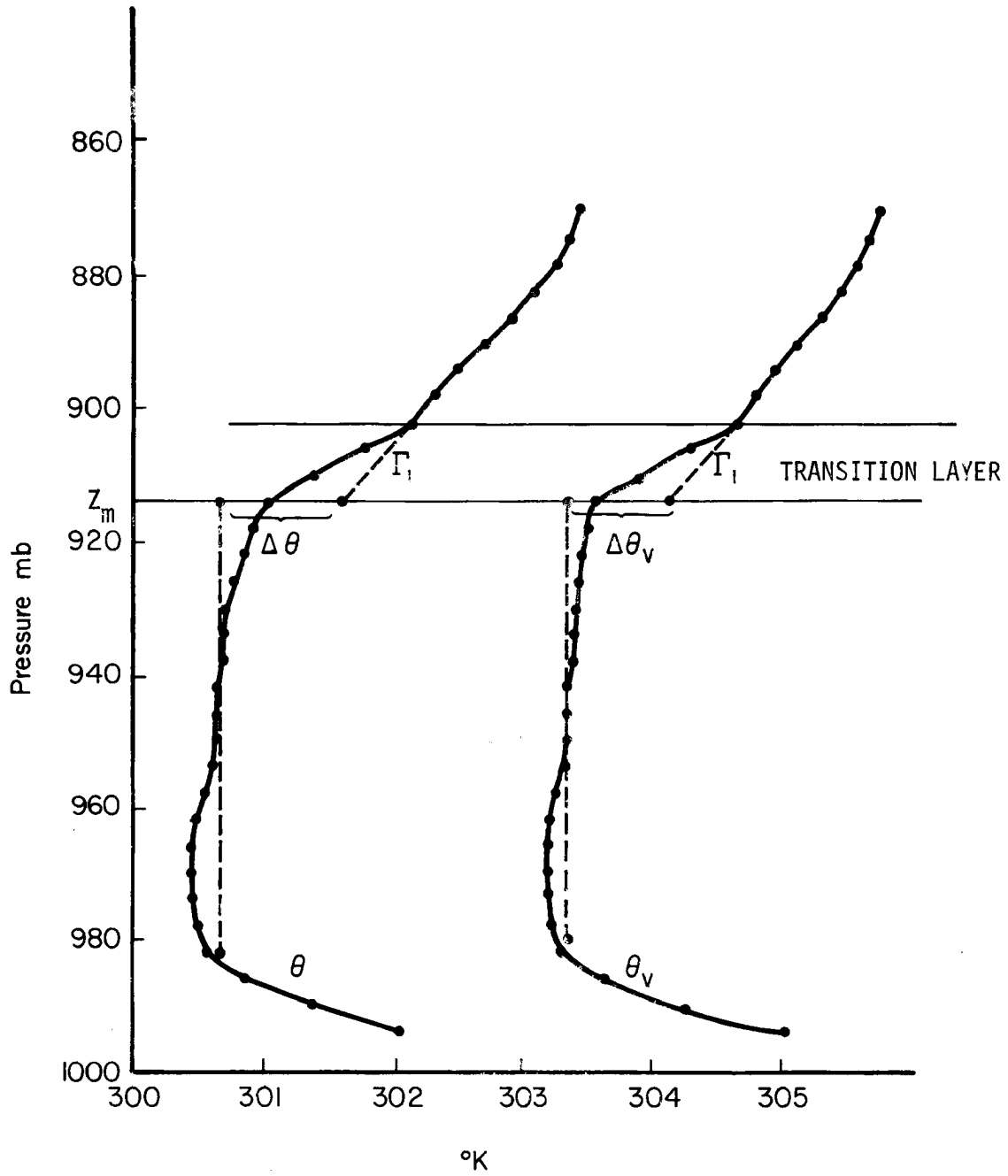


Figure 3.2 - Average of selected sondes scaled by observed transition layer base, TL#1.

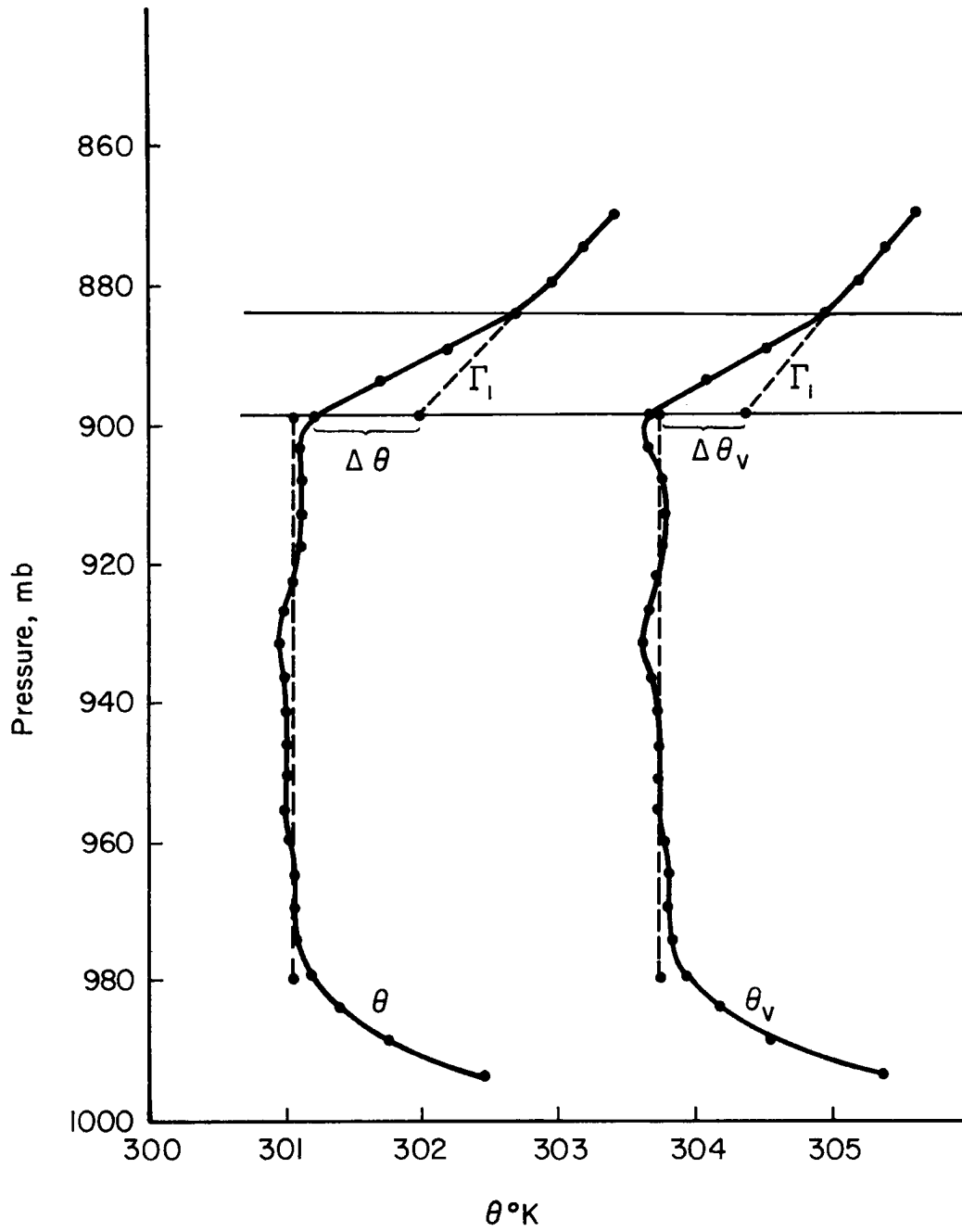


Figure 3.3 - Average of selected sondes scaled by observed transition layer base, TL#2.

sondes. The inversion strength ($\Delta\theta$, $\Delta\theta_v$) for the finite transition layer is determined by extrapolating the lapse rate, Γ_1 , down to the base of the transition layer and subtracting the mean potential temperature in the mixed layer from this value (see Fig. 3.2; Betts, 1974a). The mixed layer was taken to be the layer from $p^* = .2$ to $p^* = 1.0$. Values of k indicated in Table 3.1 were obtained from equation 3.2 using both θ and θ_v profiles.

TABLE 3.1
CALCULATED VALUES OF k FROM
SELECTED SONDES SCALED BY TRANSITION LAYER BASE

SOURCE	Γ_1	$\Delta\theta$	k	Z_m meters	Γ_1	$\Delta\theta_v$	k
	$^{\circ}\text{K}/\text{km}$	$^{\circ}\text{K}$			$^{\circ}\text{K}/\text{km}$	$^{\circ}\text{K}$	
TL1	4.92	.93	.26	919	4.01	.74	.25
TL2	4.82	.95	.23	1068	4.39	.63	.16

The rather small range of k is encouraging and agrees with other estimates by Tennekes (1973) and Deardorff, et al (1974). These results indicate a significant amount (approximately 20%) of the enthalpy flux which enters the sub-cloud layer from the top of the layer.

4. CUMULUS LAYER

4.1 Description

The tropical atmosphere has a large requirement to transport heat vertically through its sixteen kilometer depth to balance the radiational cooling. The large-scale effect of precipitation is a net warming of the atmosphere, although locally, clouds may cool their environment (Gray, 1972).

Non-precipitating convection can also modify the environment through selective source and sink regions for liquid water. There is no net warming of the atmosphere in this process (if $L(T)$ variation is neglected). This process with entrainment (and detrainment) is not isentropic, thus there is a change in the distribution of potential temperature with respect to mass.

Figure 4.1 represents the thermodynamics of the tropical non-precipitating cumulus layer. $\theta(e)$ represents a typical environmental stratification. The curve $\theta_{es}(p)$ depicts the parcel path for an entraining cloud parcel. The parcel is assumed to carry all its liquid water with it. This buoyant parcel driven by condensational heating will continue to ascend until the parcel encounters a stable layer of the atmosphere wherein the parcel loses its kinetic energy and falls back, evaporating its liquid water if this has not been precipitated. This case (see Fig. 4.1) will be examined in this thesis. After the parcel has evaporated all its liquid water, the cloud parcel will descend nearly dry adiabatically until it reaches equilibrium with its environment (Z_1). Entrainment of stably stratified air has kept the parcel from descending back to cloud base (Z_b). The foregoing discussion may also be presented employing the concept of liquid water potential temperature (Fig. 4.1).

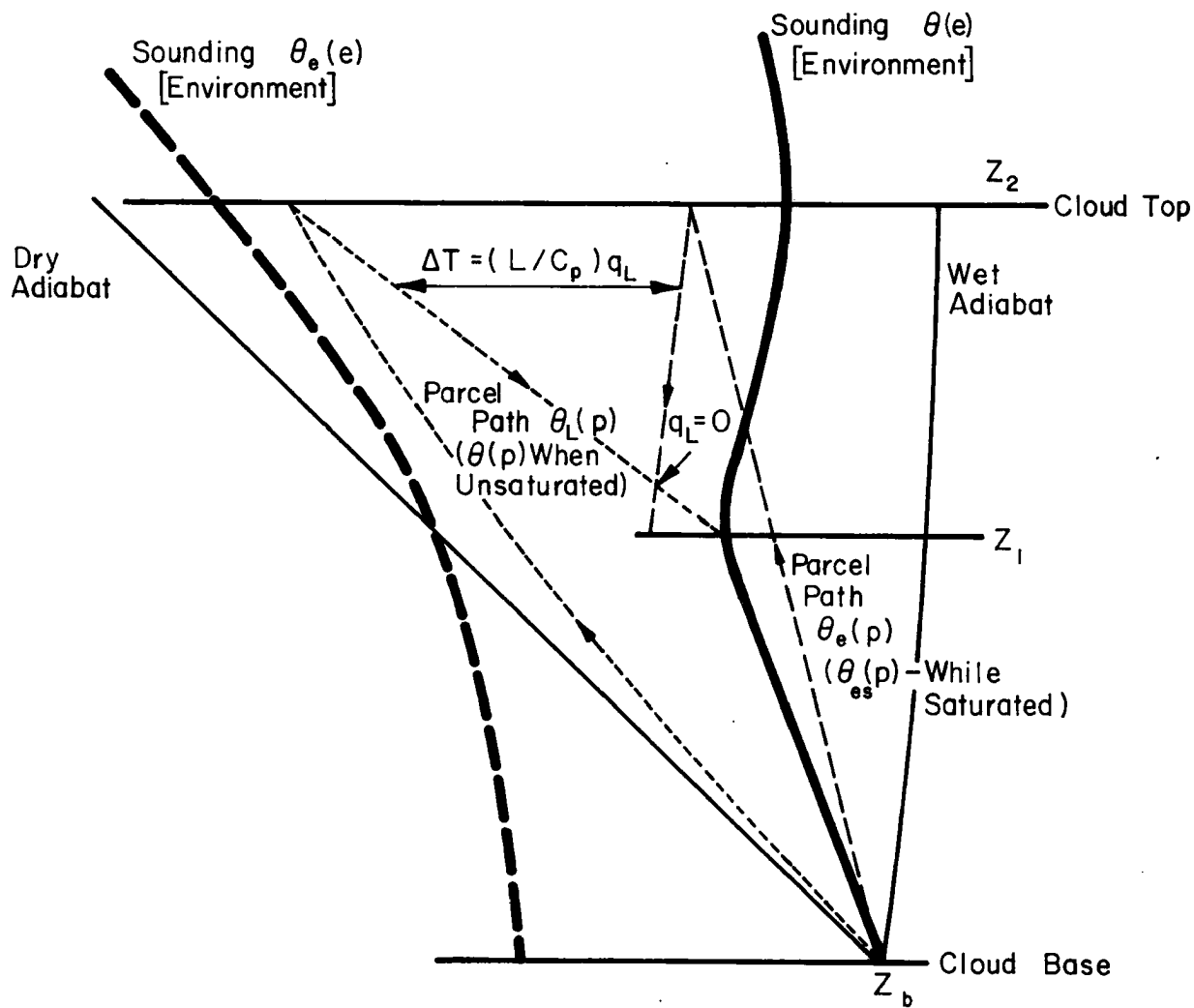


Figure 4.1 - Sketch tephigram through cumulus layer depicting typical parcel paths ($\theta_e(p)$, $\theta_{es}(p)$ and $\theta(p)$, $\theta_L(p)$) for a cloud parcel diluting with its environment. θ_e and θ_{es} values are read off the wet adiabats while θ_L and θ values are read off the dry adiabats, from Betts (1973a).

At cloud base $\theta_L(p)$ is assumed equal to $\theta(e)$ (temperature perturbation neglected). As the cloud parcel rises condensing liquid water, dilution with the unsaturated environmental air causes $\theta_L(p)$ to tend toward the environmental lapse-rate ($\theta(e) = \theta_L(e)$). The difference between the two dashed parcel paths is proportional to the liquid water content of the parcel; consequently, their intersection defines the level where the parcel has evaporated all its liquid water on descent. The coupling of this typical parcel path with the thermal stratification of the environment is an essential feature of the lapse-rate model to be discussed in the next section.

4.2 Lapse-Rate Model

The lapse-rate model of Betts (1973a) assumes a two-layer structure to the cumulus layer as depicted in Fig. 4.2a. The model will be used diagnostically here to predict a two-layer structure from boundary values $Z_b, \tilde{\theta}_b, Z_2, \tilde{\theta}_2$ which together define a

$$\bar{\Gamma} = \tilde{\theta}_2 - \tilde{\theta}_b / Z_2 - Z_b$$

That is the model will be used to predict Z_1, θ_1 (and therefore $\Gamma_1, \Gamma_2, \Delta Z_1, \Delta Z_2$ in Fig. 4.2a) from the boundary values, and these predicted lapse rates and layer depths will be compared with those observed (see Fig. 4.7 to 4.13).

To predict the two unknowns (conceptually Z_1, θ_1) the model uses two equations (see Appendix A), based on the ascent and descent of a typical entraining cloud parcel. The first is a kinetic energy equation shown schematically in Fig. 4.2b. The model parcel rises with entrainment and some dissipation of kinetic energy, overshoots to reach a maximum height of Z_2 (Appendix Eq. A16). The second equation is a little less obvious. The ascent and descent to thermal equilibrium of a model

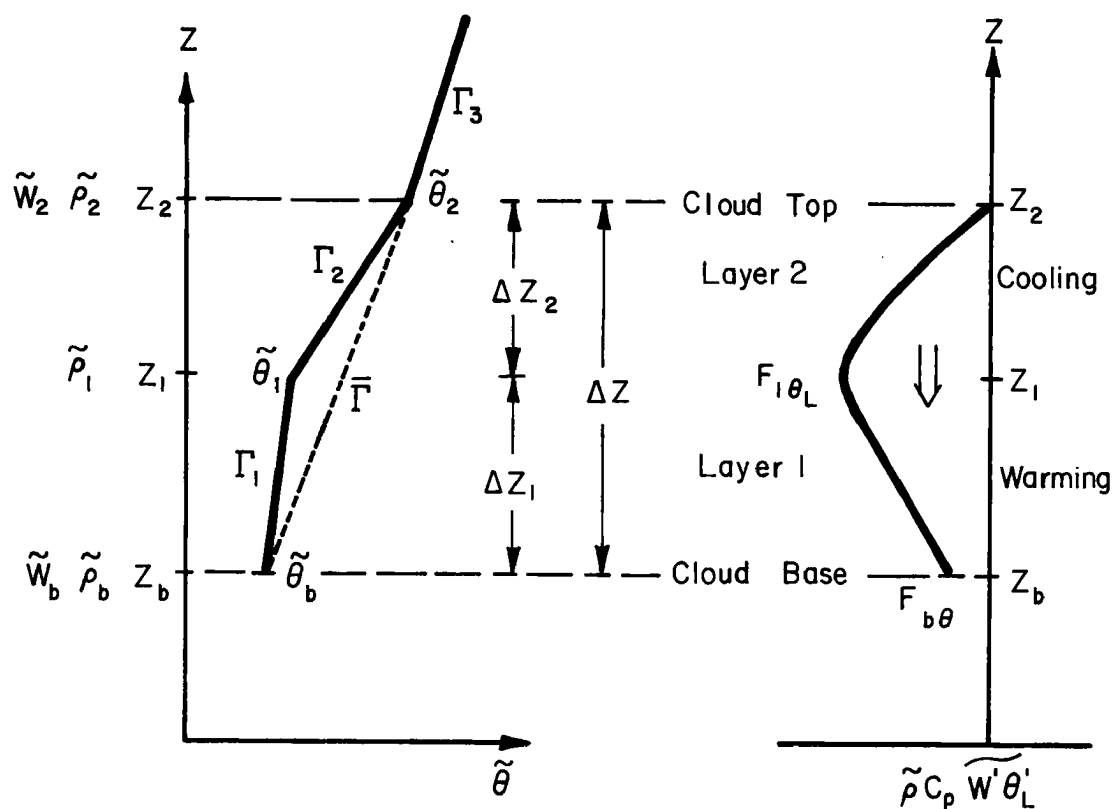


Figure 4.2a - Lapse-rate model for the cumulus layer from Betts (1973a). Heat flux profile is purely schematic.

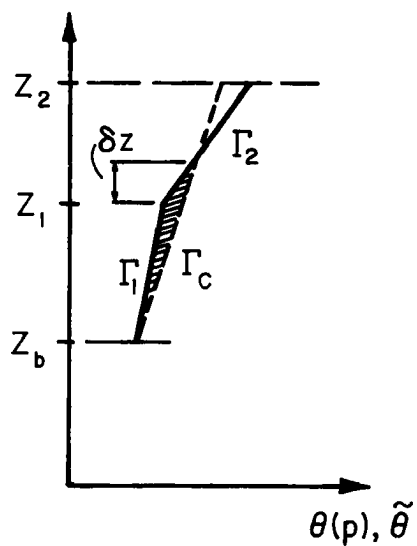


Figure 4.2b - Two-layer model stratification with cloud parcel path on ascent. Shaded region represents the maximum available positive potential energy from Betts (1973a).

parcel discussed in 4.1 in terms of its θ_L path effectively produces a downward heat transport, since all the liquid water condensed below the level Z_1 (in Fig. 4.1) is evaporated above this level. The lower layer is warmed and the upper layer cooled by this process. It seems reasonable to identify the level of change from warming to cooling as the level where the lapse-rate changes slope. Thus, if all the heat and water transports were produced by these model parcels, the equilibrium level of the parcel on descent will mark the level where Γ_1 changes to Γ_2 . This is the basic assumption of the second equation of the lapse-rate model: the parcel comes back to thermal equilibrium at Z_1 where Γ_1 changes to Γ_2 . This assumption gives Appendix Eq. A.13.

The stratification is thus coupled to a model parcel path and related to an entrainment or dilution rate of the parcel. This process of entrainment is parameterized in terms of a dilution scale length (S) where:

$$\frac{1}{S} = \frac{1}{M} \frac{dM}{dZ} = \frac{E}{Z_1} \quad (4.1)$$

The depth of the conditionally unstable layer is used to scale entrainment. An objective of the following sections is to determine approximate values for E and to test both the validity of this simple scaling relationship and the over all model. Figure 4.2b depicts the thermal stratification of the model with the shaded area corresponding to the maximum potential energy available to the cloud parcel. In general, turbulent diffusion and dilution will tend to limit the actual kinetic energy of the cloud parcel as it overshoots into the stable region. A parameter D will be used to represent that portion of the available potential energy (shaded region of Figure 4.2b) actually

realized in the form of kinetic energy of the parcel as it overshoots (see Eq. A.16). In testing the model against observational data, the parameters E, D will be varied to determine a best fit and thus the preferred values for E and D.

To summarize, the boundary conditions for the cumulus layer are assumed known. A cloud parcel is assumed to entrain at a constant rate on ascent and then on descent to Z_1 , and this parcel path is coupled to the stratification by a kinetic energy equation and a θ_L equation. However, it must be realized that although this θ_L equation is based conceptually on the heat transport by the model parcel, the equation is used here only as a constraint on the stratification, not to predict heat fluxes. In the diagnostic use of this model, the enthalpy flux shown schematically in Fig. 4.2a is not determined. This can only be done implicitly if the lapse-rate model is used prognostically with time dependent boundary conditions. Then as the lapse-rates change in balance with the large-scale varying fields, the convective heat transports are implicitly specified (see Betts, 1973a).

The following section discusses the nature of solutions to the model.

4.3 Numerical Solutions of the Lapse-Rate Model

In this section, the lapse-rate model is solved for a large range of assumed values applicable to the tropical atmosphere in an effort to study the characteristics of the model.

The input parameters were varied in the following manner (see Fig. 4.2 and symbol list):

$$\bar{\Gamma}: \quad 10^{\circ} \text{ K/km to } 3^{\circ} \text{ K/km}$$

$$\Gamma_c: \quad 5.5^{\circ} \text{ K/km to } 2.5^{\circ} \text{ K/km}$$

E: 0.8 to 0.3

D: 1.0 to 0.2

Values of Γ_1 , Γ_2 , ΔZ_1 , ΔZ_2 were obtained.

Unique solutions existed for all $\bar{\Gamma} > \Gamma_c$, implying that the solutions satisfy the inequality $\Gamma_2 > \bar{\Gamma} > \Gamma_c > \Gamma_1$. Since the parcel's temperature perturbation and vertical velocity are neglected at cloud base, $\bar{\Gamma} > \Gamma_c$ is a necessary condition for a solution to exist. The tests indicate that this is also a sufficient condition.

Figures 4.3-4.6 indicate the functional dependence of Γ_1 , Γ_2 , $\frac{\Delta Z_1}{\Delta Z_2}$, and $\frac{\Gamma_1}{\Gamma_2}$ on $\bar{\Gamma}$ for a wide range of parcel lapse-rates (Γ_c) with $E = .45$, $D = .60$. Second degree polynomials describe Γ_1 and Γ_2 as a function of $\bar{\Gamma}$ while $\frac{\Delta Z_1}{\Delta Z_2}$ shows a linear dependence on $\bar{\Gamma}$ (Γ_c held constant).

The solutions (Figs. 4.3-4.6) indicate that as $\bar{\Gamma} - \Gamma_c$ increases, Γ_1 slowly decreases, Γ_2 increases rapidly, and $\frac{\Delta Z_1}{\Delta Z_2}$ increases. For large values of $\bar{\Gamma} - \Gamma_c$ a strong inversion results, and an error in the value of $\bar{\Gamma} - \Gamma_c$ has pronounced effects on the calculated value of Γ_2 , but only a minor impact on the value of Γ_1 . The reverse is the case for small $\bar{\Gamma} - \Gamma_c$.

These solutions were obtained with $E = .45$ and $D = .60$. The observational evidence (section 4.5) indicates these are representative values for the entrainment and kinetic energy dissipation parameters, respectively. The next section discusses the effects on the model resulting from specified variations in these parameters.

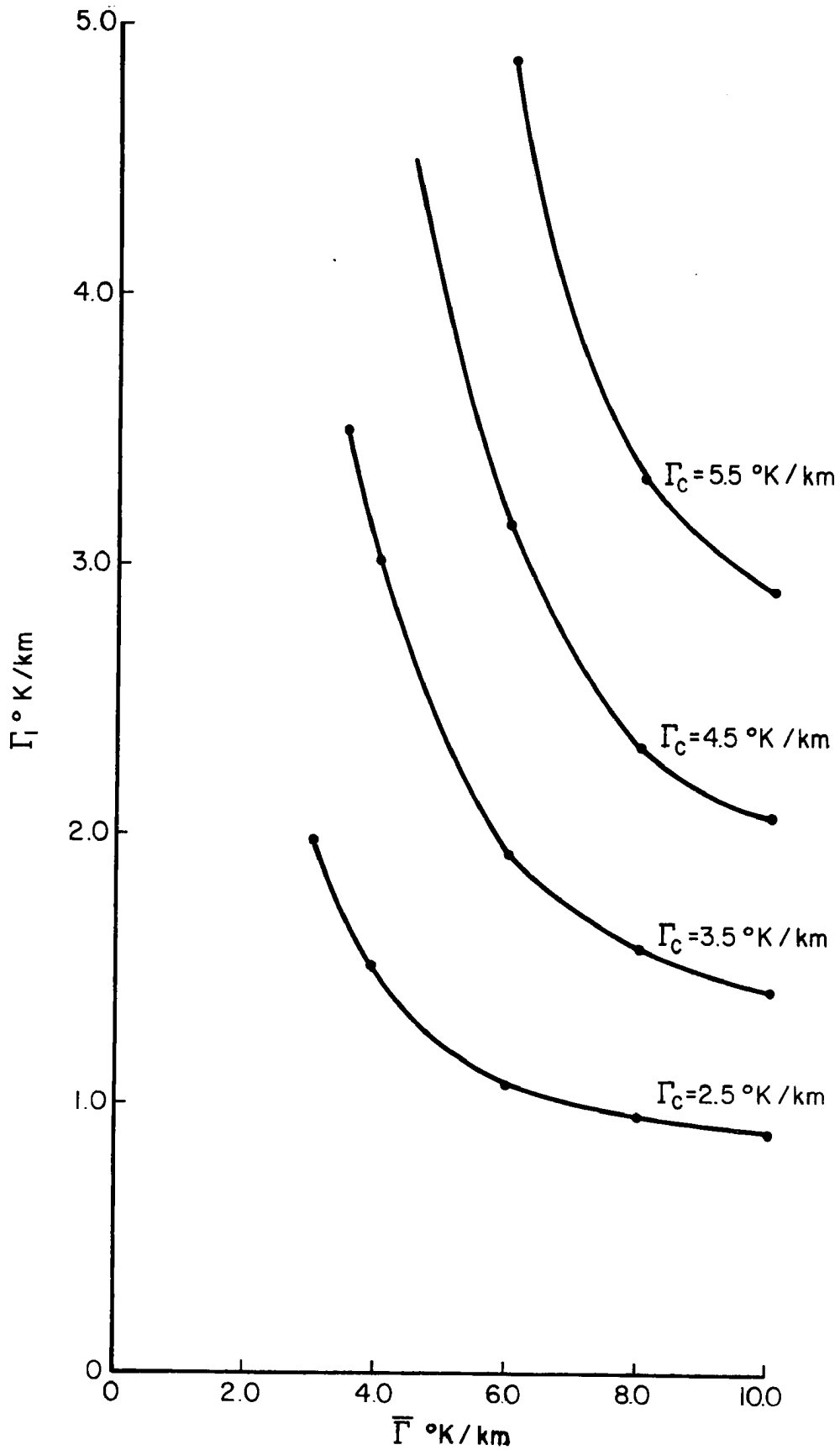


Fig.4.3 - Model calculations of $\Gamma_1 = f(\bar{\Gamma})$ for various cloud parcel lapse rates (Γ_c) and mean stratification ($\bar{\Gamma}$) for $E = .45$, $D = .60$.

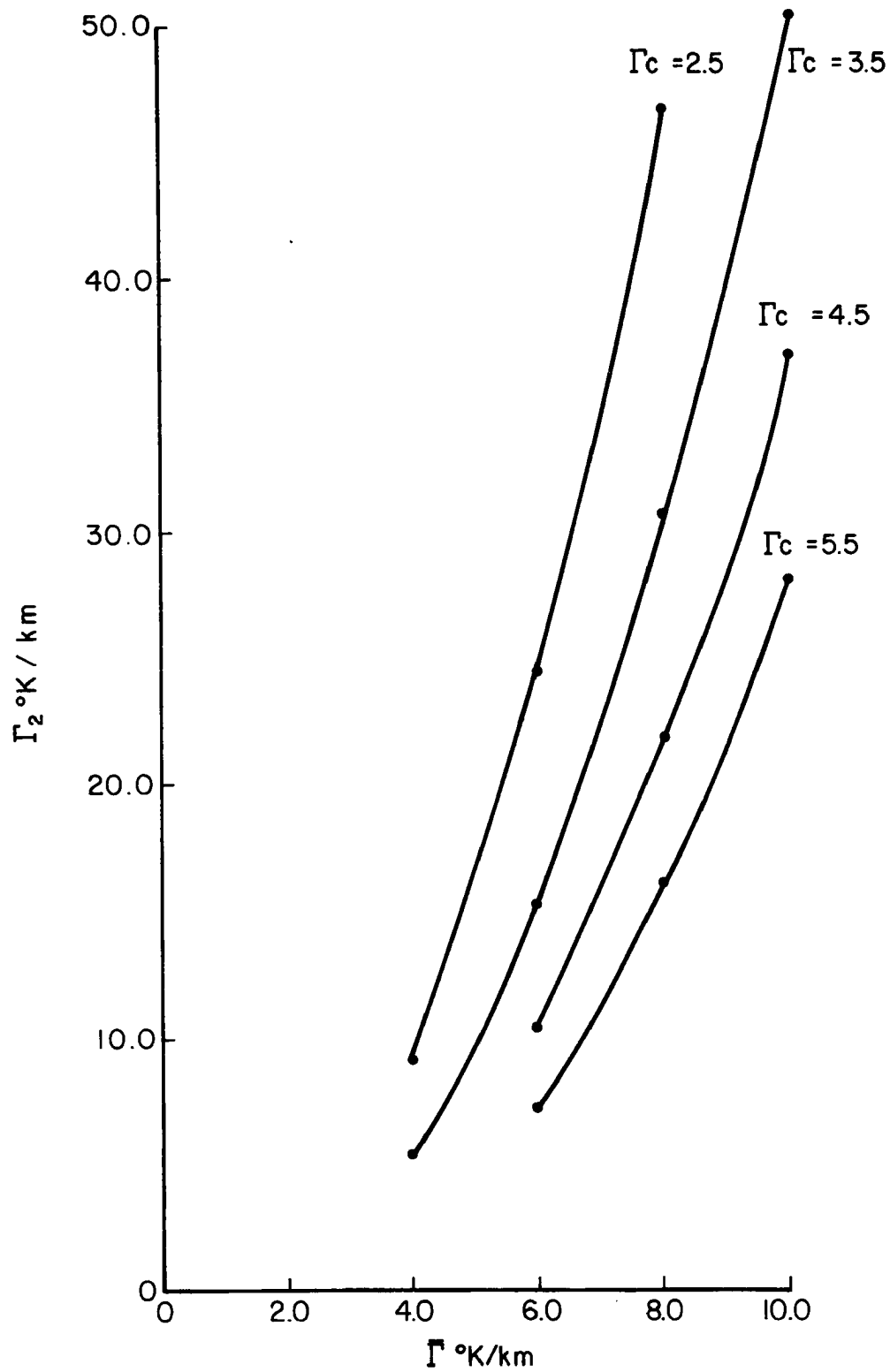


Figure 4.4 - Model calculations of $\Gamma_2 = f(\Gamma)$ for various cloud parcel lapse-rates (Γ_c) and mean stratification (Γ) for $E = .45$, $D = .60$.

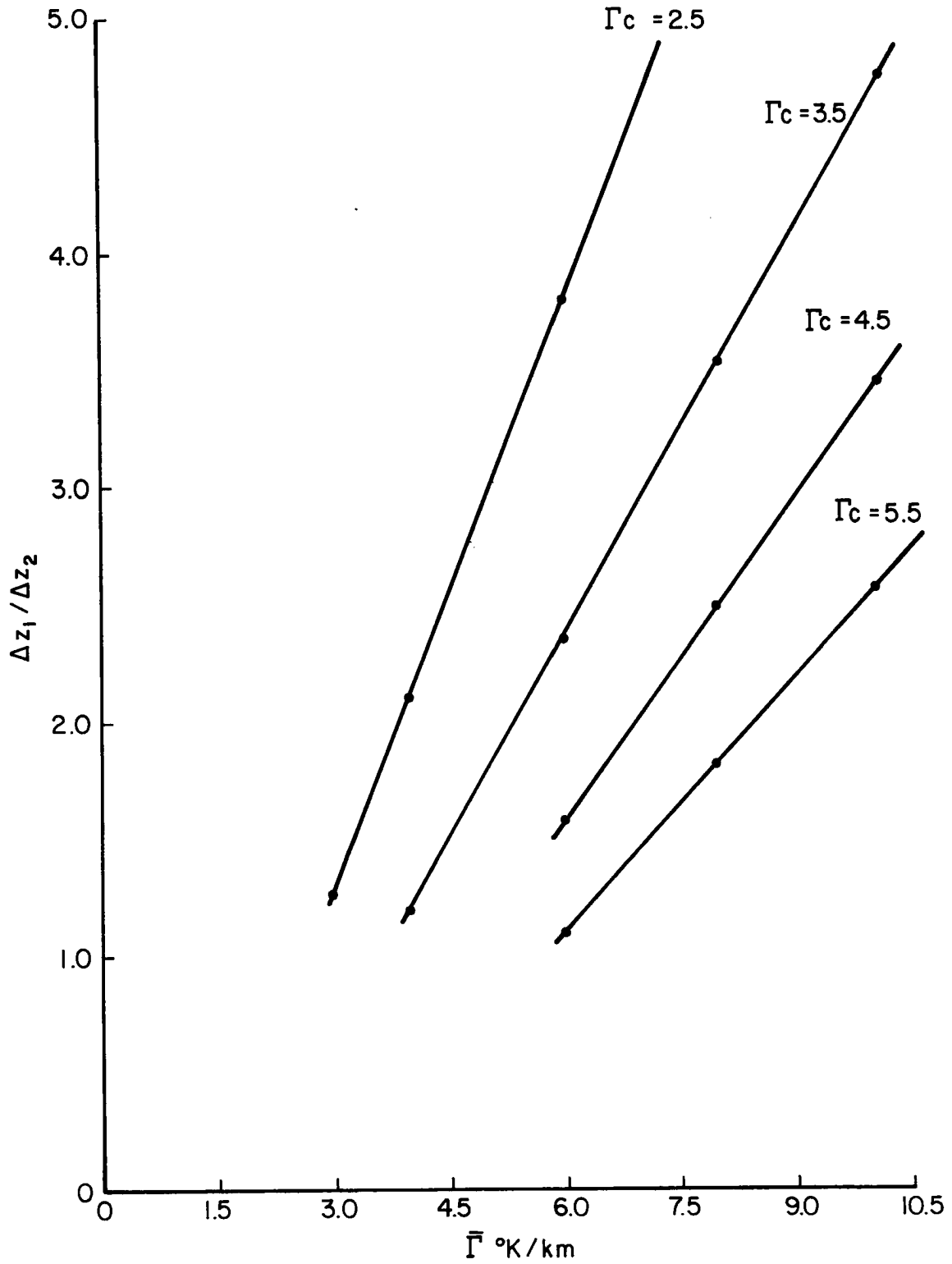


Figure 4.5 - Model calculations of $\Delta z_1 / \Delta z_2 = f(\bar{\Gamma})$ for various cloud parcel lapse-rates (Γ_c) and mean stratification ($\bar{\Gamma}$) for $E = .45$, $D = .60$.

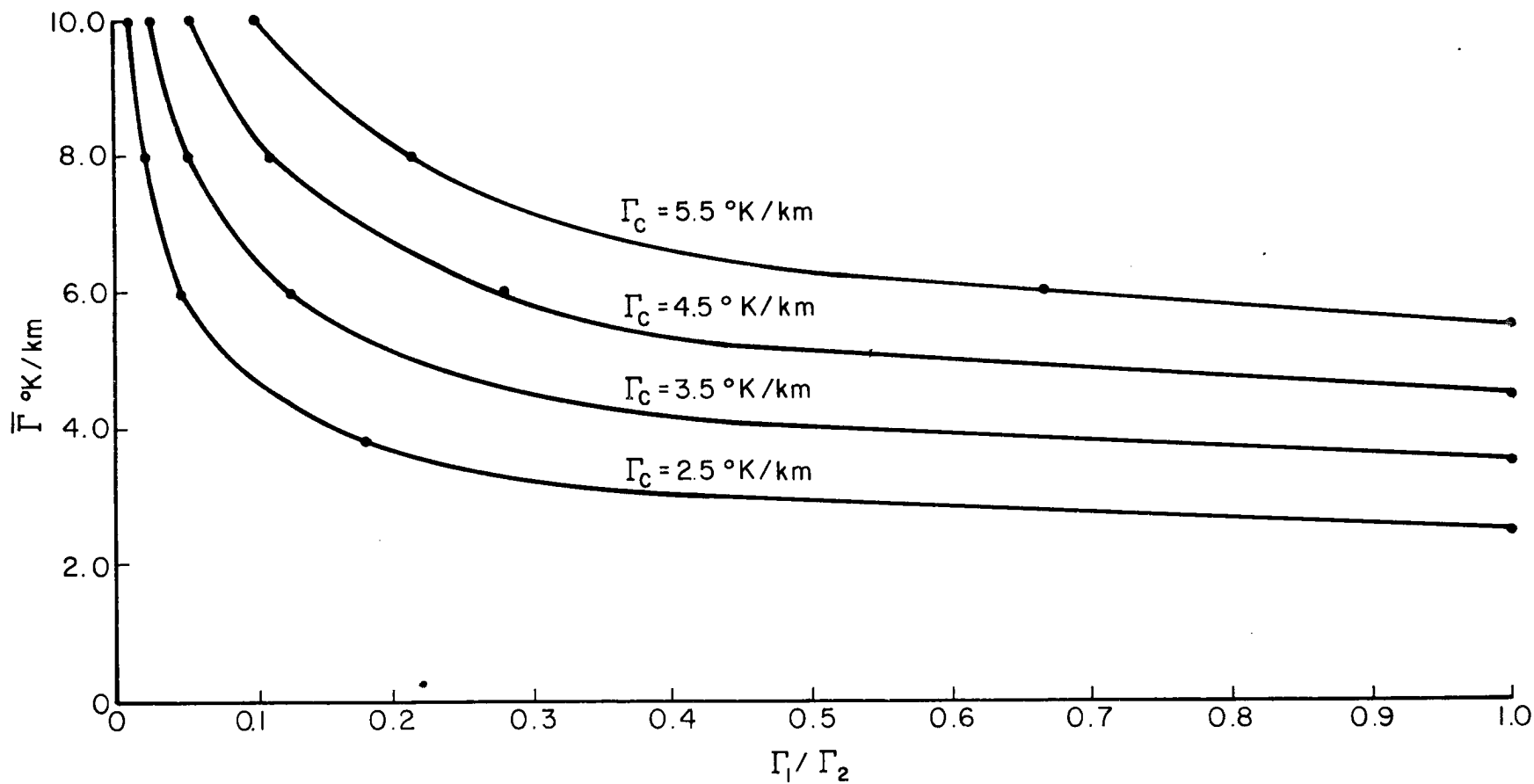


Figure 4.6 - Model calculations of $\Gamma_1/\Gamma_2 = f(\bar{\Gamma})$ for various cloud parcel lapse-rates (Γ_c) and mean stratification ($\bar{\Gamma}$) for $E = .45$, $D = .60$.

4.4 Sensitivity Tests of Lapse-Rate Model

A sensitivity analysis was performed on the model with the parameters E and D varied from reference values of E = .45, D = .60. The parcel lapse-rate (Γ_c) was held constant at 4.5⁰K/km. Table 4.1 indicates the percent changes in Γ_1 , Γ_2 , and $\frac{\Delta Z_1}{\Delta Z_2}$ for changes in E and/or D of ± 0.1 . The values given are with respect to the reference state and for $\bar{\Gamma} = 10^0$ K/km or 6⁰K/km.

TABLE 4.1
SENSITIVITY ANALYSIS OF LAPSE-RATE MODEL PARAMETERS

VARIATION OF E and/or D	Γ_1	Γ_2	$\frac{\Delta Z_1}{\Delta Z_2}$	Change
	%	%	%	
E = .45 \pm .10	\pm 5.50	\pm 13.90	\pm 18.45	$\bar{\Gamma} = 10^0$ K/km
with E+D = 1.05	\pm 2.10	\pm 6.50	\pm 17.10	$\bar{\Gamma} = 6^0$ K/km
E = .45 \pm .10	\pm 12.90	\pm 8.60	\pm 11.70	$\bar{\Gamma} = 10^0$ K/km
D = .60	\pm 5.70	\pm 0.03	\pm 13.90	$\bar{\Gamma} = 6^0$ K/km
E = .45	$\bar{\Gamma}$ 7.66	\pm 6.40	\pm 6.70	$\bar{\Gamma} = 10^0$ K/km
D = .60 \pm .10	$\bar{\Gamma}$ 3.65	\pm 3.00	\pm 3.20	$\bar{\Gamma} = 6^0$ K/km

Increasing E while simultaneously decreasing D such that E + D remains constant result in small changes in Γ_1 but substantial changes in Γ_2 and $\frac{\Delta Z_1}{\Delta Z_2}$. Increasing the dilution parameter (E) increases the values of Γ_1 , Γ_2 , and $\frac{\Delta Z_1}{\Delta Z_2}$ while increasing D decreases Γ_1 but increases Γ_2 and $\frac{\Delta Z_1}{\Delta Z_2}$.

In general, the sensitivity of the model to changes in E or D increases as $\bar{\Gamma} - \Gamma_c$ increases. For the most part, changes of $\pm .1$ in E and/or D result in five to fifteen percent changes in the models' results. Therefore, if observational evidence predicts reasonably constant values for E and D, the model will yield useful results without the necessity to vary E and D to fit the data.

4.5 Model Comparisons with Observational Data.

4.5.1 Determination of Input Parameters (see model in Appendix A)

The lapse-rate model was solved using observational data from BOMEX, ATEX, and VIMHEX II. Cloud base was specified as the top of the transition layer (if well-defined). In the absence of a well-defined transition layer (several VIMHEX II cases), cloud base is estimated as the lowest LCL in the sub-cloud region (Dugan, 1973). Z_1 is designated as the level with the minimum value of θ_{es} in the cumulus layer, while Z_2 is designated as the level with the maximum value of θ_{es} in the stable layer. Table 4.2 indicates how these levels were found for an example profile.

Data was only available at specified levels (section 2.1) from ATEX. Z_1 was designated as the top of the conditionally unstable layer ($Z_1 = Z_{ib}$: minimum value of θ_{es}). Two runs of the model were made for each case with Z_2 specified by Z_{ict} and Z_{it} (see 2.1). In all cases but one, $Z_2 = Z_{ict}$ gave the best results (section 4.5.2).

The parameters Γ_w , R, and J (see Appendix A) were defined as the average values in the conditionally unstable layer (ΔZ_1). Table 4.3 indicates the input values for each case. The dilution and kinetic energy dissipation parameters E and D were varied from 0.2 to 0.8 to see which values gave the best fit.

TABLE 4.2
 AVERAGE OF SOUNDINGS 1300-1500 LOCAL STANDARD TIME
 DURING SUPPRESSED CONVECTION

PRESS (mb)	HEIGHT (meters)	T TEMP (°C)	r MIX g/kg	θ TH °K	θ_e TH-E °K	θ_{es} TH-ES °K
990	198	31.5	15.0	305.6	350.2	398.3
975	337	29.2	14.4	304.6	347.3	385.9
950	568	26.4	13.8	304.0	344.7	373.8
925	802	24.2	13.4	304.1	343.9	366.6
900	1042	22.2	13.3	304.4	343.7	361.1
875	1287	20.2	12.8	304.8	342.8	356.2
→ 850	1537	18.1	11.6	305.2	339.8	351.6
825	1792	16.1	11.1	305.6	338.7	347.6
800	2054	14.0	11.1	306.1	339.5	344.1
775	2322	12.2	10.3	307.0	337.8	341.8
750	2597	10.8	8.8	308.4	335.0	341.5 ←
725	2879	9.8	7.2	310.2	332.4	342.5
700	3171	9.0	6.0	312.5	331.3	344.6
675	3472	7.9	4.9	314.5	329.9	345.5 ←
650	3782	6.3	3.9	316.2	328.8	345.2
625	4103	4.4	4.1	317.5	330.6	344.1
600	4435	2.6	3.1	319.2	329.3	343.8

Average LCL: 837 mb

Z_b : 1664 meters

Z_1 : 2597 meters

Z_2 : 3472 meters

TABLE 4.3
INPUT VALUES FOR LAPSE-RATE MODEL CALCULATIONS

SOURCE	ΔZ meters	$\bar{\Gamma}$ °K/km	$\bar{\Gamma}_w$ °K/km	$r_s - r_e$ g/kg	J	R/J °K
BOMEX - Average	1580	5.58	5.80	2.7	3.6	1.855
ATEX - MET 1	955	7.64	5.73	2.5	3.45	1.81
MET 2	1617	6.31	5.70	1.5	3.34	1.34
PLA 1	922	10.40	5.55	1.7	2.9	1.47
PLA 2	800	10.50	5.60	1.6	3.0	.93
VIMHEX						
Avg. 1300L-1500L	1808	5.03	5.53	2.7	2.7	2.50
Avg. 1700L-1900L	3591	4.96	5.60	3.8	2.36	4.00
SONDE # 39	1328	6.33	5.53	2.0	2.6	1.92
42	1144	5.94	5.80	1.8	2.76	1.65
53	3527	5.47	5.70	3.0	3.00	2.50
65	1545	5.44	5.65	3.0	2.9	2.57
105	1106	5.42	5.70	2.7	2.7	2.50
108	2625	5.75	5.75	3.8	2.49	3.82
111	2195	5.74	5.70	2.1	3.0	1.75
113	1383	4.92	5.65	4.0	2.5	4.00
146	2656	5.54	5.75	3.0	2.5	3.00
201	2762	4.89	5.50	3.7	2.45	3.74
211	3589	5.00	5.47	3.3	2.40	3.44
230	2366	4.99	5.60	3.3	2.9	2.59
253	1494	4.95	5.70	3.1	2.8	2.32
260	2078	4.91	5.65	2.1	2.7	1.95
302	2379	5.38	5.65	2.5	2.4	2.60
328	1953	5.53	5.65	2.5	2.5	2.50

4.5.2 Results of the Lapse-Rate Model

The model yielded unique solutions in all cases as $\bar{\Gamma} > \Gamma_c$. Table 4.4 indicates the observed thermal structure and the "best fit" model results for each case. These "best fit" results were obtained by minimizing the fractional errors of both Γ_1/Γ_2 and $\Delta Z_1/\Delta Z_2$ where the fractional error is defined as:

$$\frac{(\quad)\text{model} - (\quad)\text{observed}}{(\quad)\text{observed}}$$

The corresponding values of E and D were designed as the "best" values for these parameters. Figures 4.7 - 4.13 indicate the observed thermal structure of the non-precipitating cumulus layer with the "best fit" model results superimposed. The general agreement is apparent. Figure 4.14 is a histogram of $\bar{\Gamma} - \Gamma_c$ and is a measure of the range of thermal structures sampled.

The model seems to somewhat underestimate Γ_1/Γ_2 for the oceanic cases (Table 4.4), however, the VIMHEX II results indicated no such trend. The height of the trade inversion varied by 20-30 mb during the five-day undisturbed period of BOMEX. The smoothing induced by averaging these sondes with respect to pressure offers a partial explanation of why Γ_1/Γ_2 is so much greater for the BOMEX average than for any of the ATEX averages. The ATEX data indicates $\Gamma_1/\Gamma_2 < .35$ for each case, while for sixteen of the eighteen land cases, $\frac{\Gamma_1}{\Gamma_2} > .40$ (Fig. 4.15). Values of $\frac{\Gamma_1}{\Gamma_2}$ of .10 to .20 are indicative of the thermal structure beneath the trade inversion while a value of .50 is representative of non-precipitating convection over land.

TABLE 4.4
COMPARISON OF MODEL RESULTS TO OBSERVED VALUES

	OBSERVED				MODEL "BEST FIT"				E/D
	Γ_1	Γ_2	$\frac{\Delta z_1}{\Delta z_2}$	$\frac{\Gamma_1}{\Gamma_2}$	Γ_1	Γ_2	$\frac{\Delta z_1}{\Delta z_2}$	$\frac{\Gamma_1}{\Gamma_2}$	
BOMEX	3.96	7.36	1.19	.54	3.99	7.5	1.18	.53	.425/.60
ATEX									
MET 1	3.38	20.0	3.9	.17	2.54	20.6	2.54	.12	.50/.60
MET 2	3.8	12.15	2.34	.31	3.59	12.3	2.21	.29	.70/.40
PLA 1	2.5	28.65	2.27	.09	2.12	30.1	2.38	.07	.30/.80
PLA 2	2.61	26.52	2.03	.10	2.27	29.1	2.26	.08	.30/.80
VIMHEX II									
Avg. 13L-15L	3.22	6.97	1.07	.46	3.65	6.7	1.20	.54	.45/.60
Avg. 17L-19L	3.88	6.22	1.17	.62	3.86	6.11	1.05	.63	.50/.60
Sonde 39	2.92	10.8	1.31	.27	2.97	11.0	1.40	.27	.35/.60
# 42	4.06	7.79	.98	.52	3.76	8.11	1.00	.46	.30/.80
53	4.5	6.71	1.28	.67	4.49	6.72	1.28	.67	.55/.60
65	4.08	6.84	1.03	.60	3.74	6.85	.83	.55	.25/.80
105	2.3	8.67	1.04	.26	2.96	8.42	1.24	.35	.35/.60
108	4.84	6.98	1.35	.69	3.54	8.5	1.26	.42	.40/.60
111	4.95	6.49	.95	.76	4.32	6.98	.88	.62	.30/.60
113	2.15	9.17	1.54	.23	2.46	8.79	1.57	.28	.425/.60
146	4.8	6.27	1.01	.77	4.14	6.92	.98	.60	.35/.60
201	3.03	6.75	1.01	.49	3.73	6.25	1.16	.60	.45/.60
211	3.00	7.34	1.19	.41	4.10	6.08	1.19	.67	.50/.60
230	3.57	6.67	1.19	.54	3.85	6.64	1.44	.58	.60/.40
253	3.9	6.64	1.61	.59	3.65	6.64	1.30	.55	.50/.60
260	3.27	6.29	.84	.52	4.52	5.33	1.07	.85	.50/.60
302	3.87	6.49	.73	.60	4.22	6.37	.85	.66	.30/.60
328	4.14	7.46	1.39	.55	3.72	7.66	1.18	.49	.40/.60
UNITS	$^{\circ}\text{K/km}$	$^{\circ}\text{K/km}$			$^{\circ}\text{K/km}$	$^{\circ}\text{K/km}$			

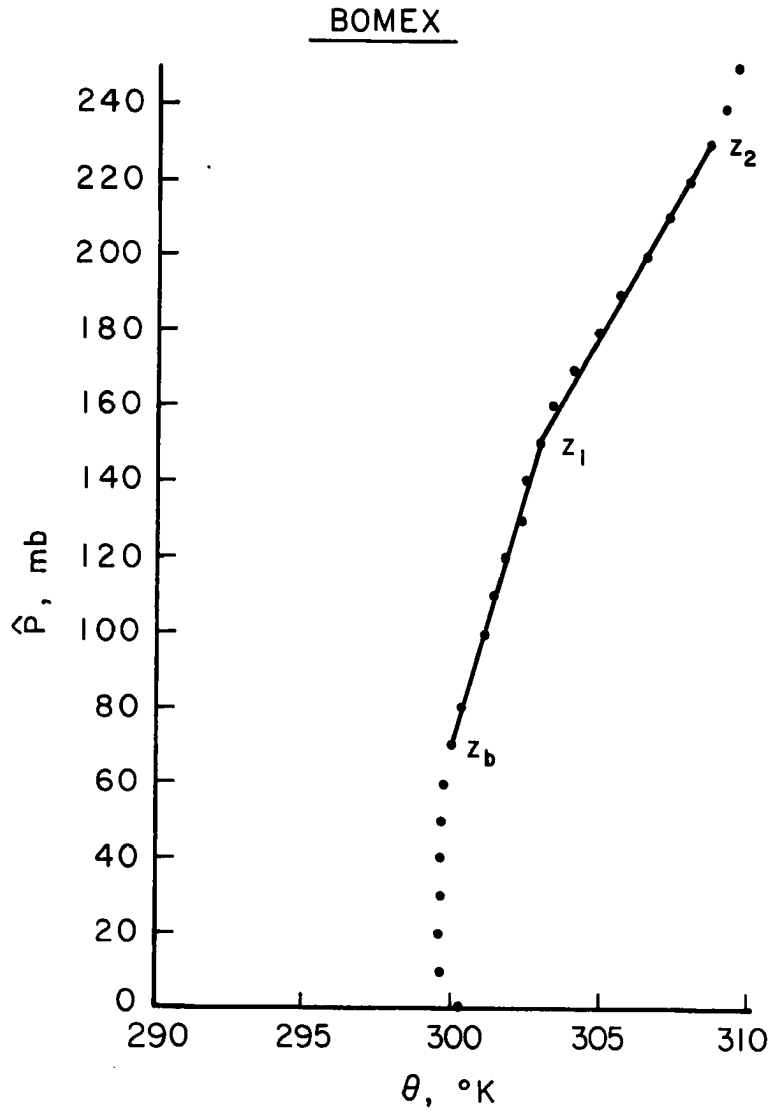


Figure 4.7 - BOMEX sounding with lapse-rate model solution superimposed (Holland and Rasmusson, 1973). Dots are data points, straight lines are lapse rates predicted by the model.

ATEX

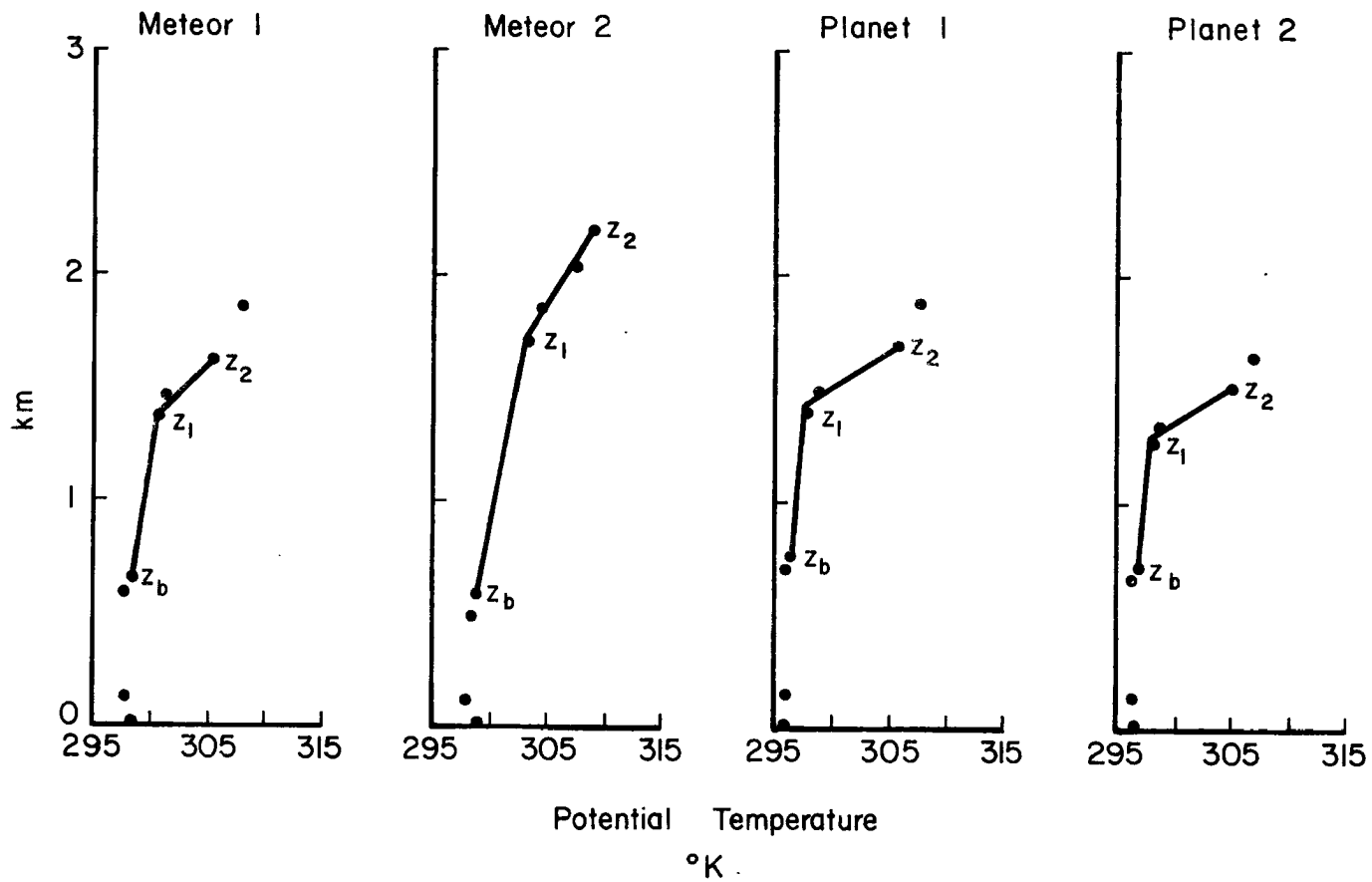


Figure 4.8 - ATEX sounding with lapse-rate model solution superimposed (Augstein et al, 1973). Dots are data levels (see section 2.1 and Fig. 2.1).

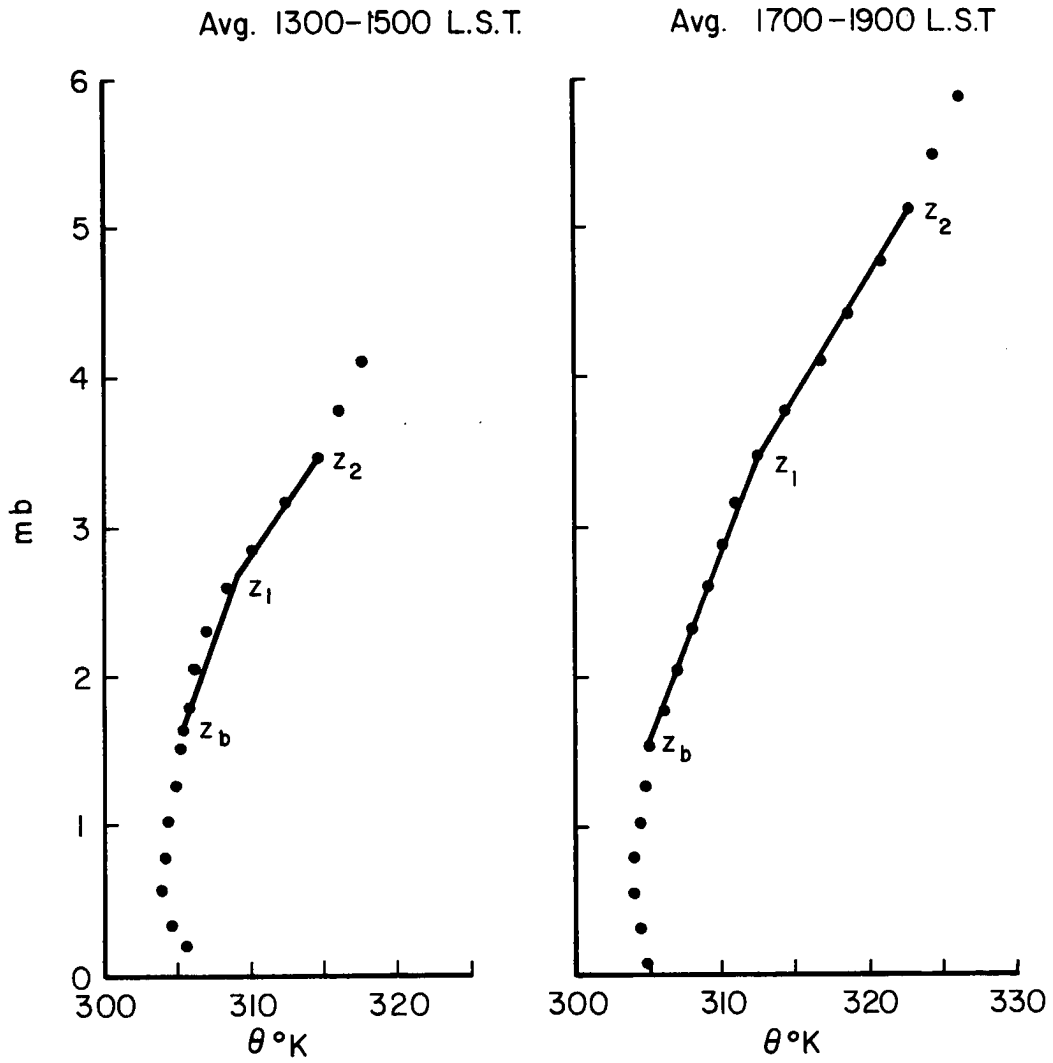


Figure 4.9 Time averaged VIMHEX II sondes with lapse-rate model solution superimposed

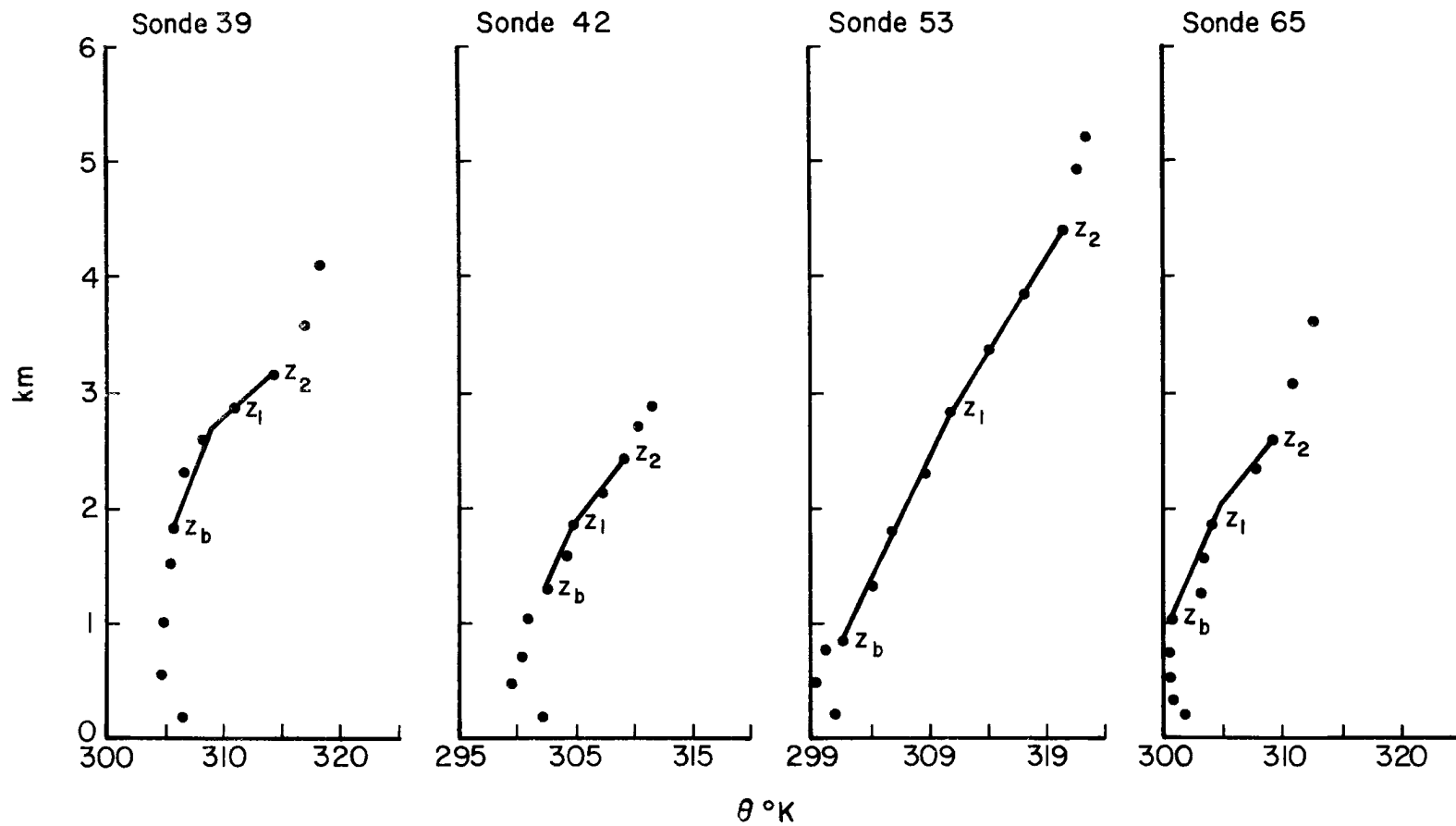


Figure 4.10 - VIMHEX II sondes 39, 42, 53, 65 with lapse-rate model solution superimposed.

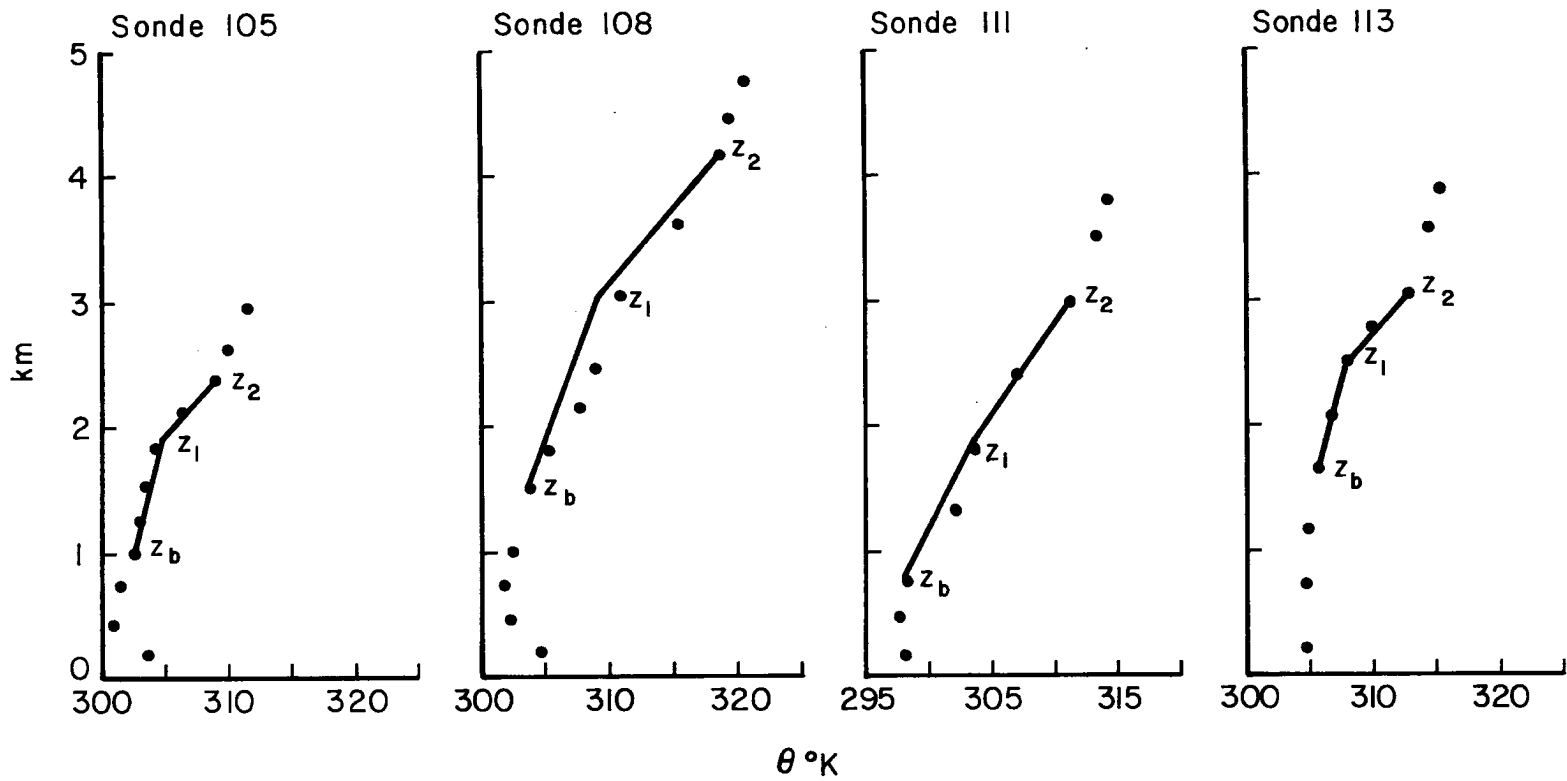


Figure 4.11 - VIMHEX II sondes 105, 108, 111, 113 with lapse-rate model solution superimposed.

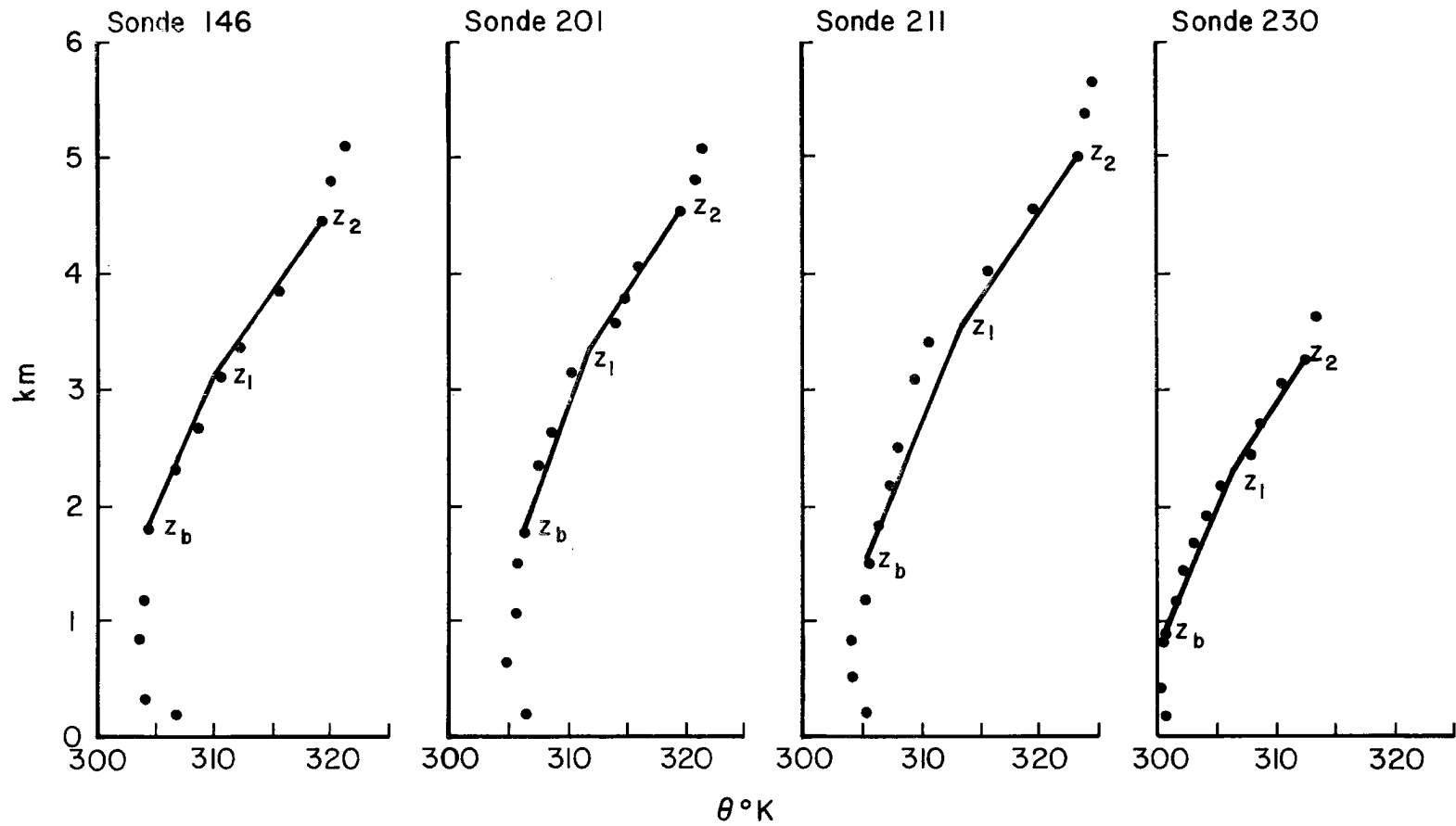


Figure 4.12 - VIMHEX II sondes 146, 201, 211, 230 with lapse-rate model solution superimposed.

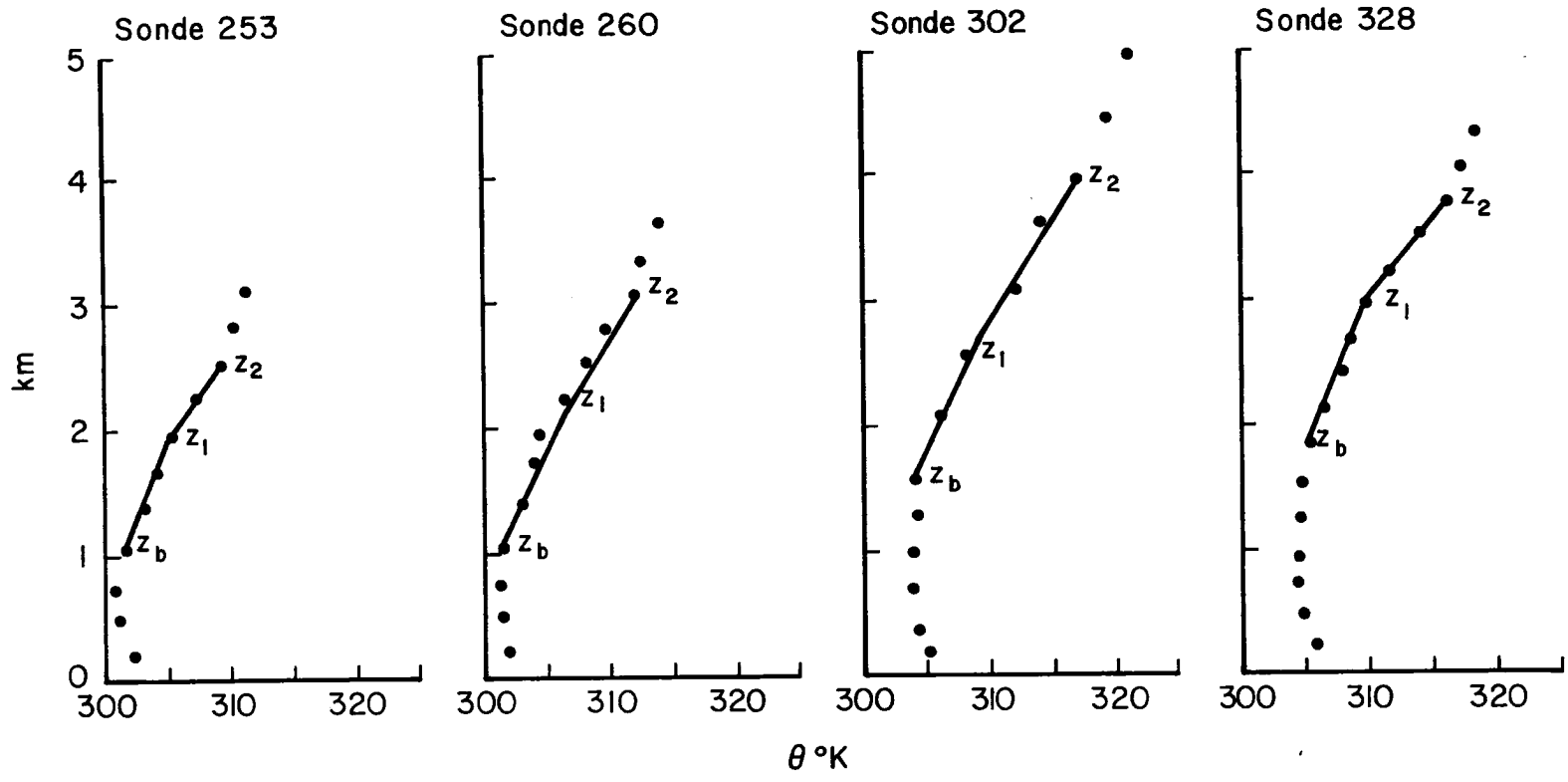


Figure 4.13 - VIMHEX II sondes 253, 260, 302, 328 with lapse-rate model solution superimposed.

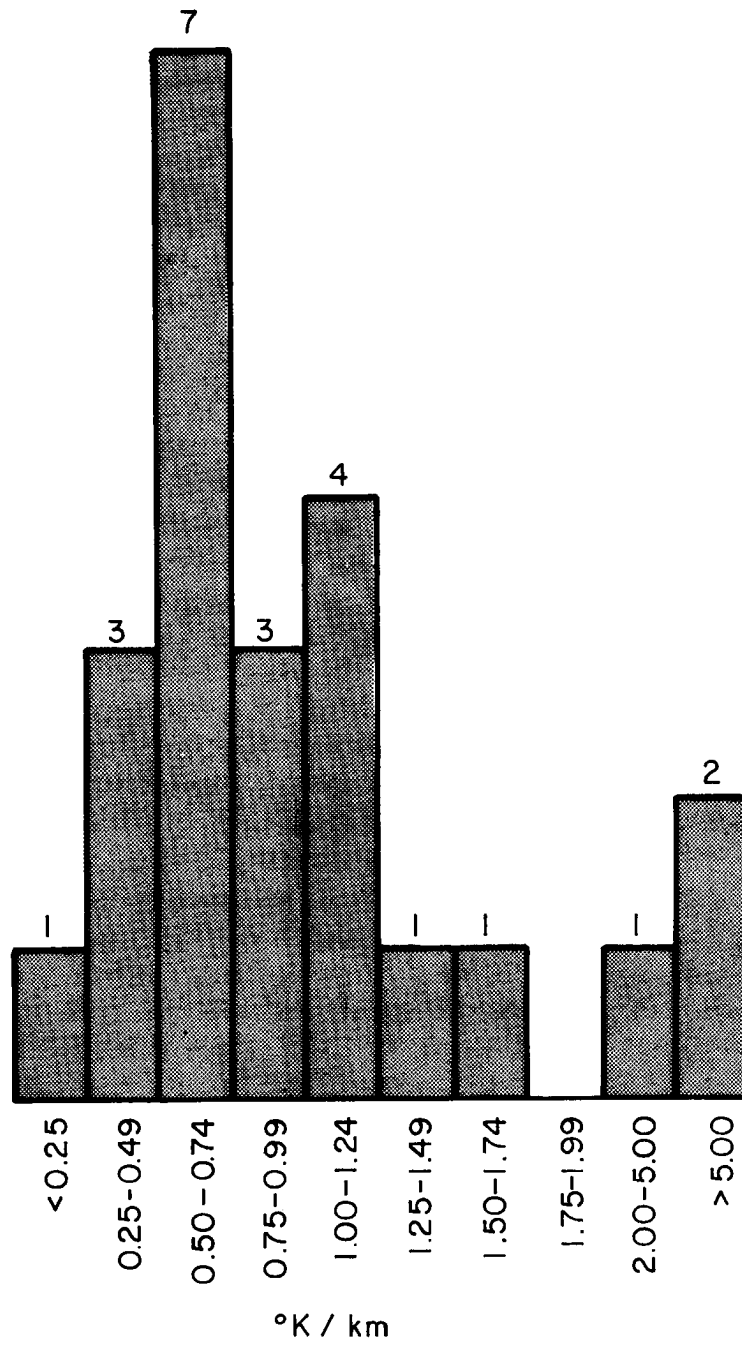


Figure 4.14 - Histogram of $\bar{\Gamma} - \Gamma_c$ for all cases tested.

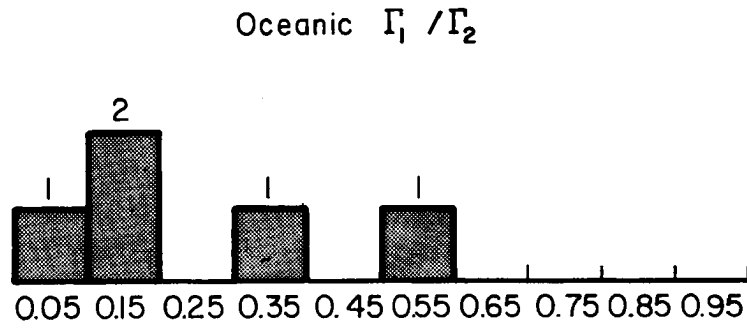
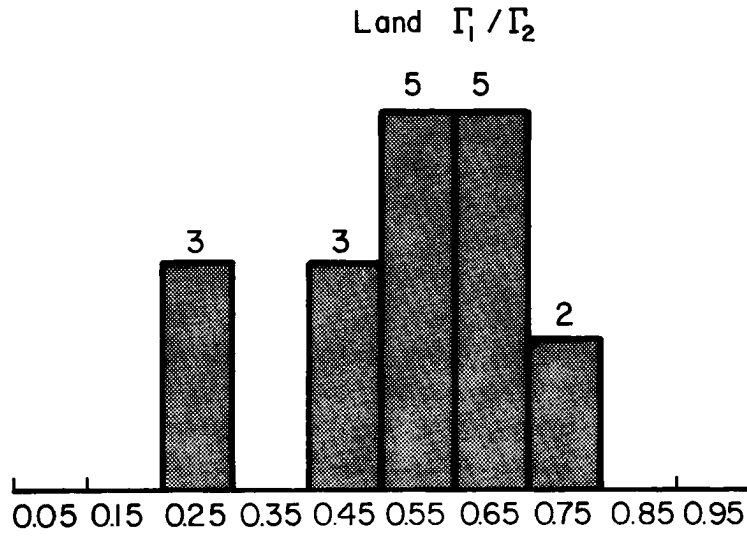


Figure 4.15 - Observed Γ_1 / Γ_2 ratios for land and oceanic cases.

The "best fit" model calculation of Z_1 was compared with the observed height for each case. An average absolute difference of 53 meters was calculated, representing 2.7% of the average depth ($\Delta Z = 1960$ meters) of the cumulus layer. If the model results for $E = .45$, $D = .60$ (Table 4.5) are used, a difference of 99 meters exists representing 5.1% of the average depth of the cumulus layer (ΔZ). Figure 4.16 indicates the relative error of the lapse-rates. Nearly 85% of the lapse-rates (Γ_1, Γ_2) (as determined from "best fit" results) are within 20% of the observed values. Using $E = .45$, $D = .60$, three of every four lapse-rates (Γ_1, Γ_2) are within 20% of the observed values. Thus, the model yields useful results for constant values of the dilution and kinetic energy dissipation parameters.

Figure 4.17 indicates the range of values for E and $E + D$. The small range of values for $E + D$ is an interesting feature of the model's results. As entrainment increases, kinetic energy dissipation might be expected to increase (D becomes smaller). The "best fit" results indicate such a trend with $E + D = 1.0$ to 1.1 as preferred values. While the range of E is large, $.25$ to $.70$, 83% of the cases have values from $.30$ to $.55$.

The depth of the layer of conditional instability of the MET 2 sounding coupled with the shallow, less intense stable layer indicates the possibility of a somewhat disturbed state to the atmosphere. This may provide a partial explanation of the extreme value of E as compared with the other oceanic cases.

The wind profiles of two VIMHEX II sondes (Figure 4.18) were examined in an attempt to find a causal relationship between the extreme low and high values of E and D as determined from VIMHEX II

TABLE 4.5
 MODEL CALCULATIONS FOR E = .45, D = .60

		Γ_1	Γ_2	$\frac{\Delta z_1}{\Delta z_2}$	$\frac{\Gamma_1}{\Gamma_2}$
BOMEX		3.96	7.6	1.24	.52
ATEX	MET 1	2.52	19.5	2.32	.13
	MET 2	3.8	9.84	1.41	.39
	PLA 1	2.13	39.1	3.47	.05
	PLA 2	2.33	36.8	3.23	.06
VIMHEX II	Avg. 13L-15L	3.65	6.7	1.20	.54
	Avg. 17L-19L	3.98	5.89	.93	.66
sonde #	39	2.98	12.12	1.73	.25
	42	3.48	9.49	1.44	.37
	53	4.58	6.33	1.07	.72
	65	3.29	8.47	1.40	.39
	105	2.8	9.6	1.54	.29
	108	3.49	8.71	1.40	.39
	111	4.22	7.55	1.20	.56
	113	2.41	9.13	1.67	.26
	146	4.0	7.4	1.21	.54
	201	3.73	6.25	1.16	.60
	211	4.17	5.90	1.08	.71
	230	4.20	5.85	1.07	.72
	253	3.75	6.36	1.17	.59
	260	4.63	5.2	.99	.89
	302	4.00	7.02	1.18	.57
	328	3.67	7.97	1.30	.46
UNITS		$^{\circ}\text{K}/\text{km}$	$^{\circ}\text{K}/\text{km}$		

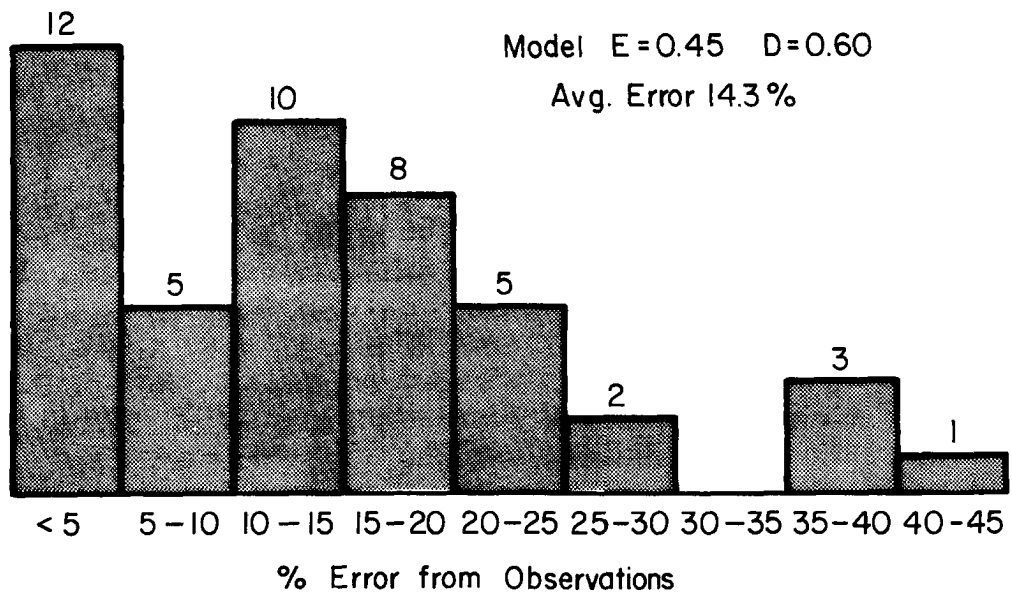
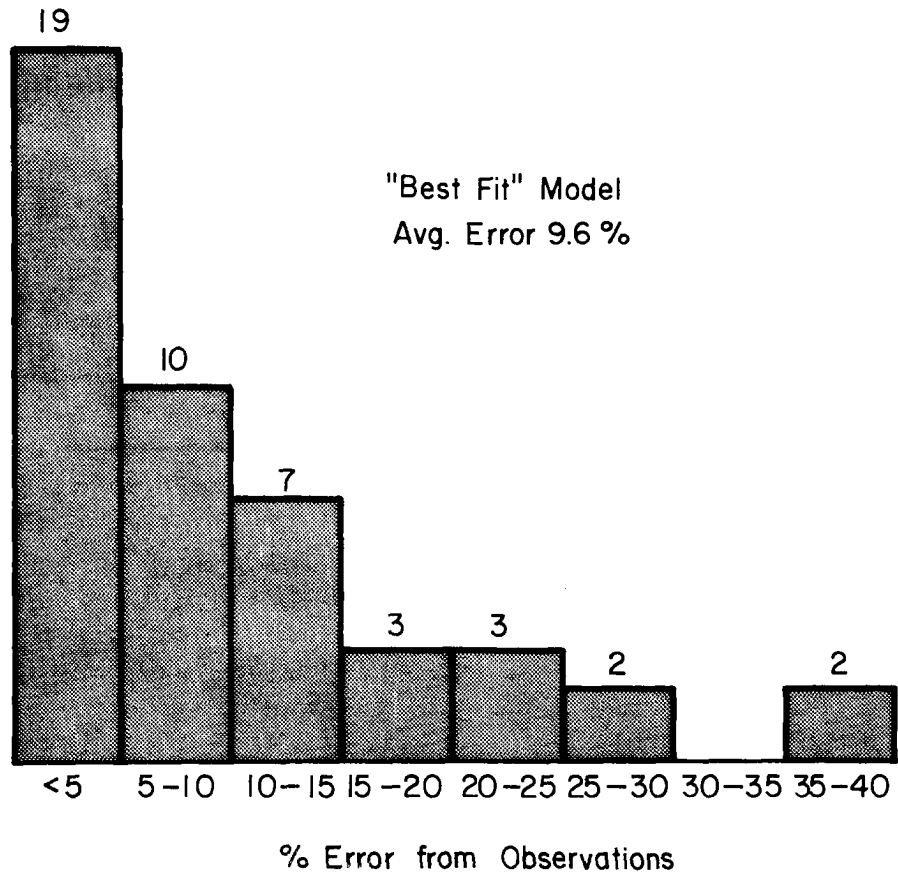


Figure 4.16 - Relative errors of lapse-rates (Γ_1, Γ_2) for the "best fit" model results and for the model results for E = .45, E = .60.

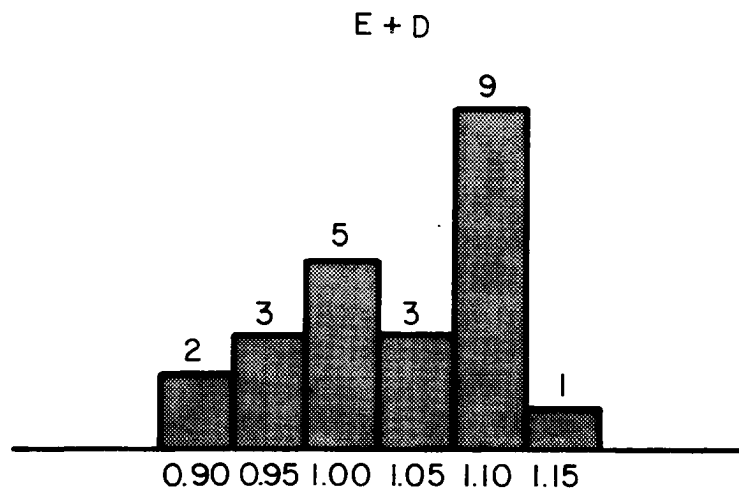
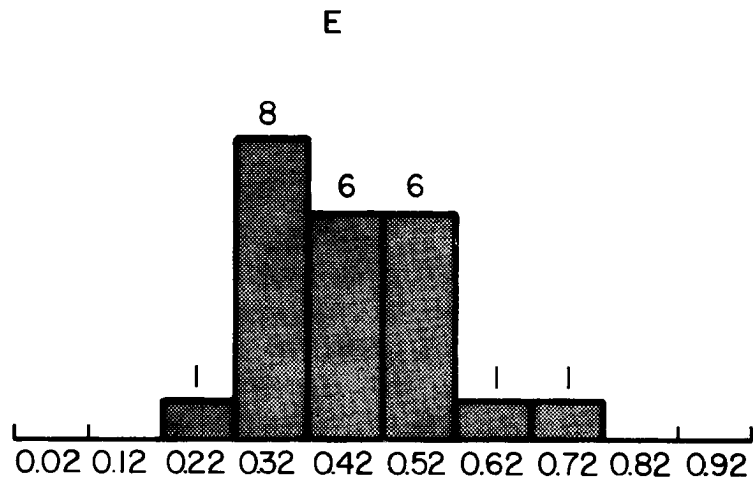


Figure 4.17 - Histogram of values for E and E + D.

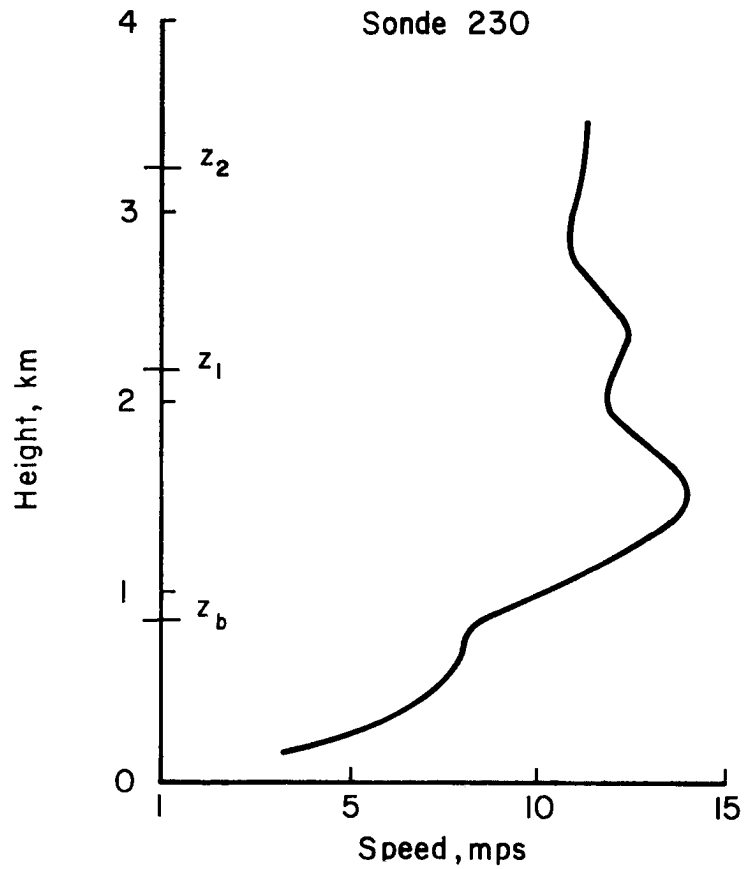
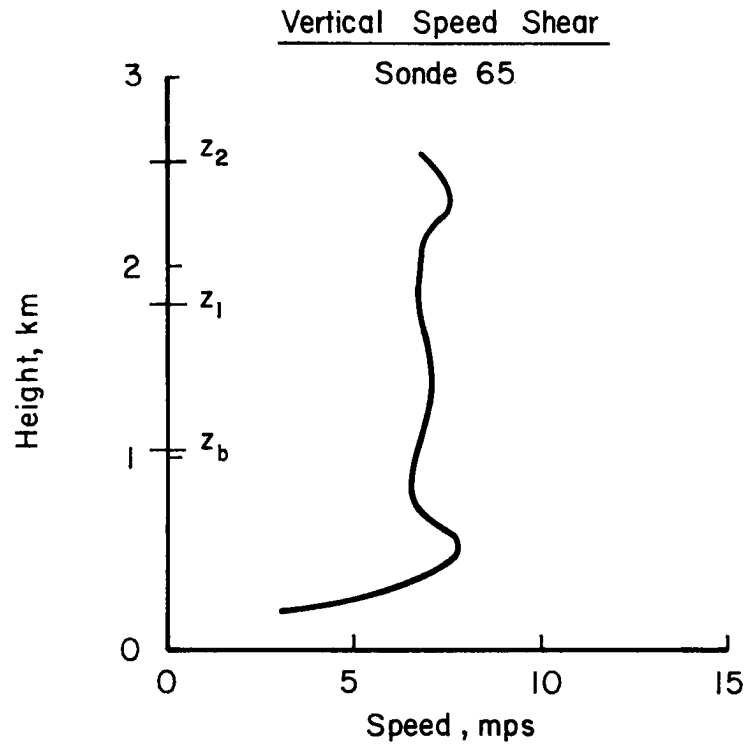


Figure 4.18 - Vertical speed shear of VIMHEX II sondes 65 and 230.

data. Kuo (1963), in a study of dry convection, showed that vertical shear has a stabilizing effect on dry convection. Steiner (1973), in a three-dimensional model of non-precipitating convection, also concluded that shear reduced convective growth. These results offer a plausible explanation for the extreme values found. The near total absence of shear through the cumulus layer in sonde 65 may have decreased the turbulent exchange between the cloud parcel and environment resulting in lower values of entrainment and kinetic energy dissipation. The strong shear evidenced from sonde 230 may be the cause of the greater dilution and kinetic energy dissipated as predicted by the model. Substituting $E = .45$ and $D = .60$ for the two sondes and assuming that the observed value of ΔZ_1 remains approximately the same, we see that the model would predict a greater depth to the cumulus layer for sonde 230 and a smaller depth for sonde 65; therefore, it appears that the vertical shear may play an important role in the parameters used in the lapse-rate model.

4.6 Determination of Dilution Scale Length from In-Cloud Radiosonde Ascents

An attempt was made to determine S (dilution scale length) from radiosondes which were observed to ascend through cloud-base. These in-cloud ascents "measure" the cloud parcel lapse-rate (see Appendix A.11)

$$\Gamma_c = \frac{d\theta_{es}(p)}{dz} = \frac{\Delta\theta_e}{S} \quad (4.5)$$

where $\Delta\theta_e = \theta_e(e) - \theta_{es}(p)$ is a measure of the degree of unsaturation of the environment. These ascents into cloud provide the values for $\theta_{es}(p)$ and $\frac{d\theta_{es}(p)}{dz}$, however, a nearly environmental stratification is needed.

In general, this would require simultaneous measurements of the in-cloud and environmental properties. Simultaneous measurements were not

available; therefore, environmental soundings were constructed by averaging sondes launched at approximately the same time of day (but not the same day) and with approximately the same LCL as the in-cloud ascents. The in-cloud ascents were grouped and averaged by the height of cloud base. The values of Γ_c and $\Delta\theta_e$ represent average values for the conditionally unstable layer. Table 4.6 indicates the values of S determined from Eq. 4.5. Using the observed depth of ΔZ_1 (Z_1 defined as θ_{es} minimum) from the environmental soundings, E was determined from $\frac{1}{S} = \frac{E}{\Delta Z_1}$.

TABLE 4.6
DILUTION SCALE LENGTH
AS DEDUCED FROM IN-CLOUD RADIOSONDE ASCENTS

	Environmental LCL890-900 mb	In-Cloud CB900-913 mb	Environmental LCL900-910 mb	In-Cloud CB913-925 mb
Number of Sondes Averaged	12	6	11	9
Average Launch Time (L.S.T.)	1018	1011	949	959
Average LCL (mb)	894.6	894.1	904.9	907.0
Γ_c ($^{\circ}\text{K}/\text{km}$)	-3.2		-2.9	
$\Delta\theta_e$ ($^{\circ}\text{K}$)	-6.6		-6.9	
S (meters)	2533		3224	
ΔZ_1 (meters)	1228		1355	
E	.48		.42	

These values for the entrainment parameter are in good agreement with the results obtained in section 4.5.2.

4.7 Parameterization of Entrainment

The parameterization of entrainment is critical to the solution of the lapse-rate model. In an attempt to determine a layer depth best associated with S , the scale dilution length, regression analyses were performed relating S to Z_2 , Z_1 , ΔZ , and ΔZ_1 . (Although in the model, S was parameterized as $\Delta Z_1/E$ (Eq. A.14), E was varied independently, so that the best fit value for E also gives a best fit value for the dilution scale, S). The observed values of Z_2 , Z_1 , ΔZ and ΔZ_1 are used in this analysis. The determination of cloud base by LCL, and the choices of Z_1 and Z_2 which specify a two-layer structure will be to some degree in error.

Correlation coefficients were determined from each data set with a range from .76 for (S, Z_1) and $(S, \Delta Z_1)$ to .86 for (S, Z_2) and $(S, \Delta Z)$. These correlation coefficients are significantly different only at the 65% confidence level for a sample size of 23 using the Fisher Z-transformation. Because of the inherent errors in the determination of S and the layer depths, two least square fits were constructed for each sample with S as the independent and then as the dependent variable (Figures 4.19-4.22). These two lines form extremes with the horizontal deviation minimized in one case and the vertical deviations in the other one. The dashed line in Fig. 4.19 is a plot of $S = \Delta Z_1/E$ through the mean values $(\bar{S}, \overline{\Delta Z_1})$. The slope indicates $S = 2.4 \Delta Z_1$ ($E = .42$).

The relatively consistent correlation coefficients suggest that ΔZ , Z_1 , or Z_2 can be used to scale entrainment as a first approximation. Suggested simple formulae for these depths are:

$$S = 1.3 \Delta Z \qquad S = 1.1 Z_1 \qquad S = .8 Z_2$$

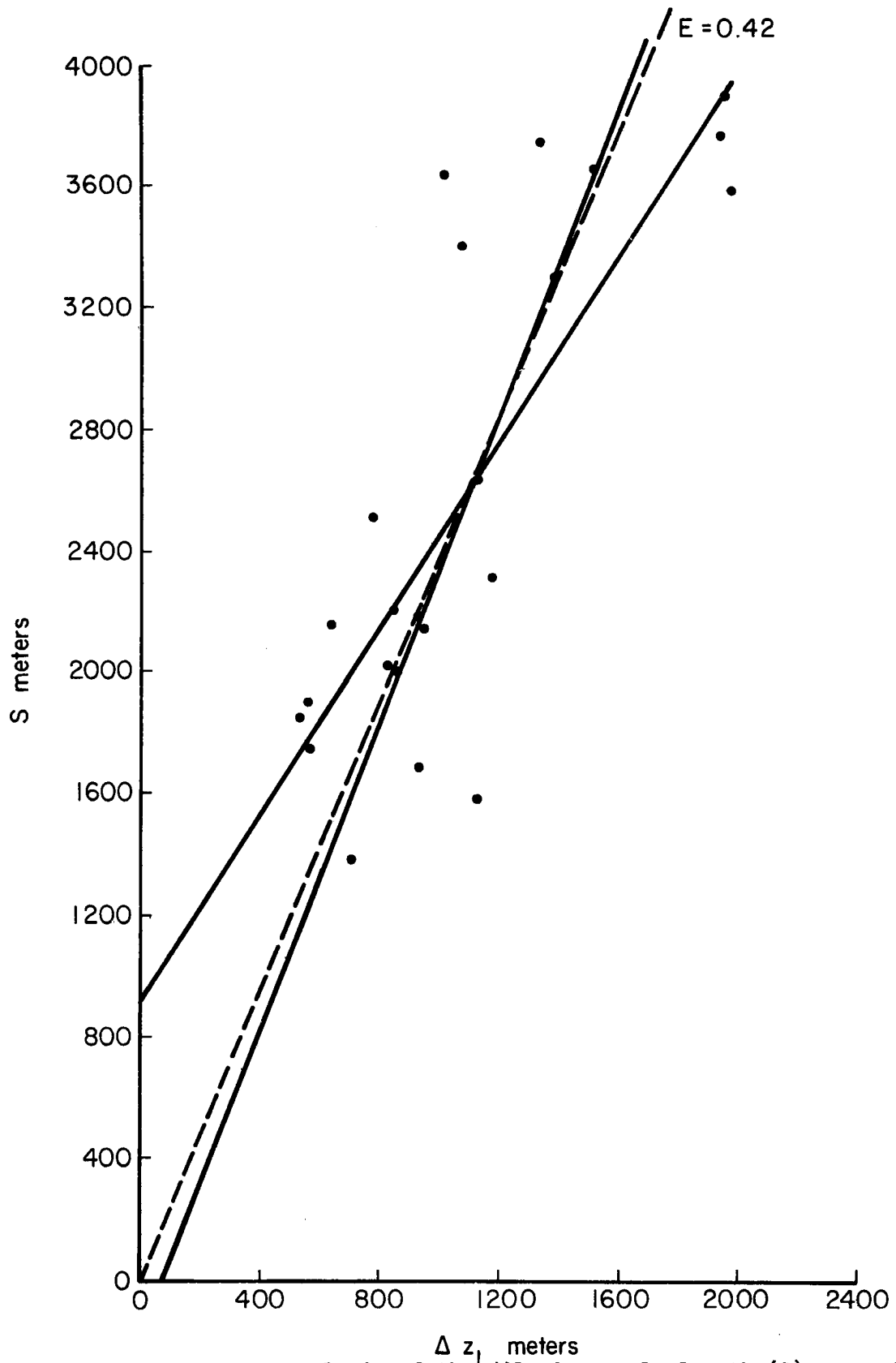


Figure 4.19 - Regression analysis of the dilution scale length (S) onto the observed value of Δz_1 . Correlation coefficient of .76. Dashed line indicates $E = .42$.

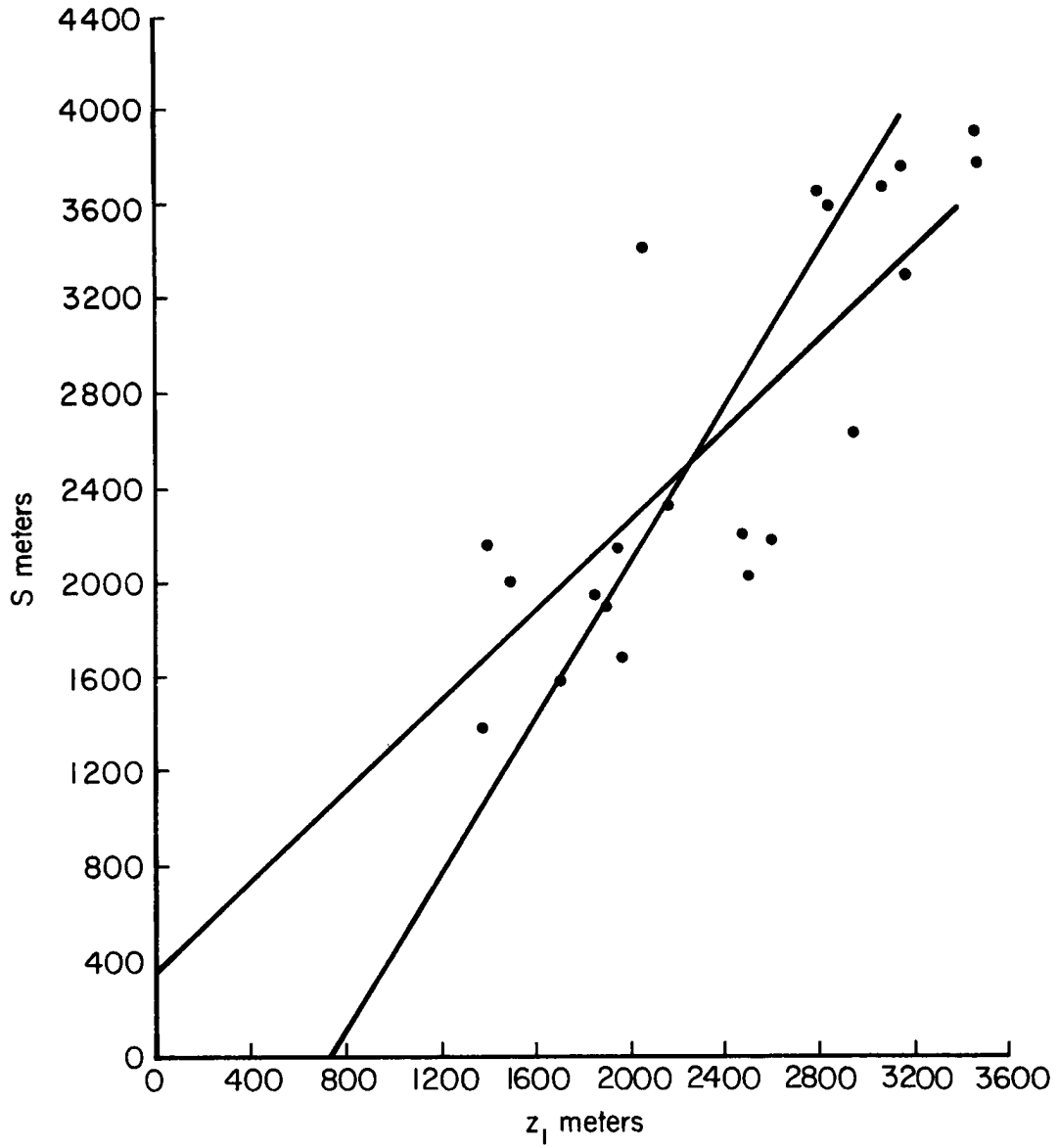


Figure 4.20 - Regression analysis of S onto Z₁. Correlation coefficient of .76.

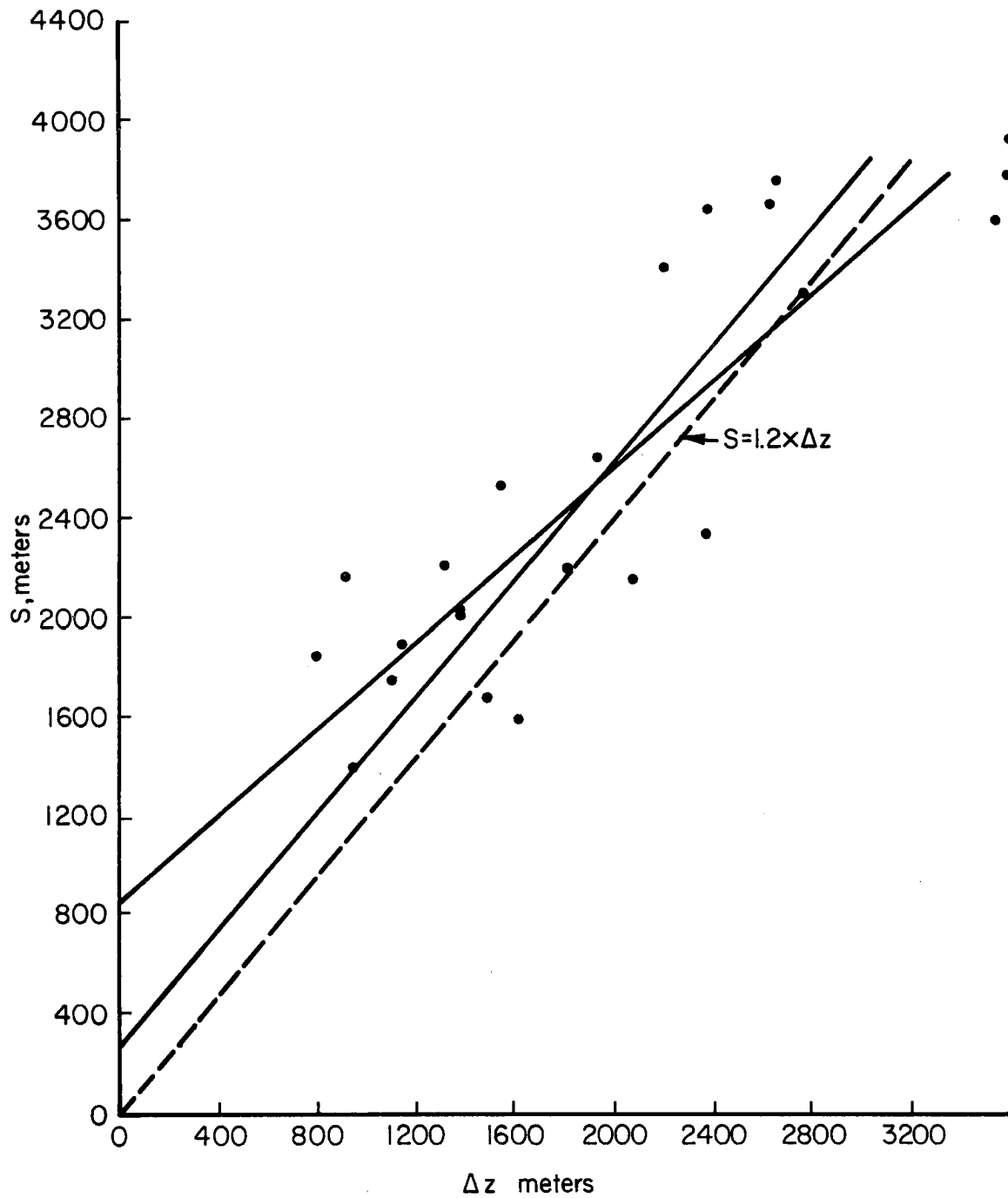


Figure 4.21 - Regression analysis of S onto ΔZ . Correlation coefficient of .86. Dashed line ($S = 1.2 \Delta Z$) corresponds to $\Delta Z/a = 6.5$ from Betts (1973b).

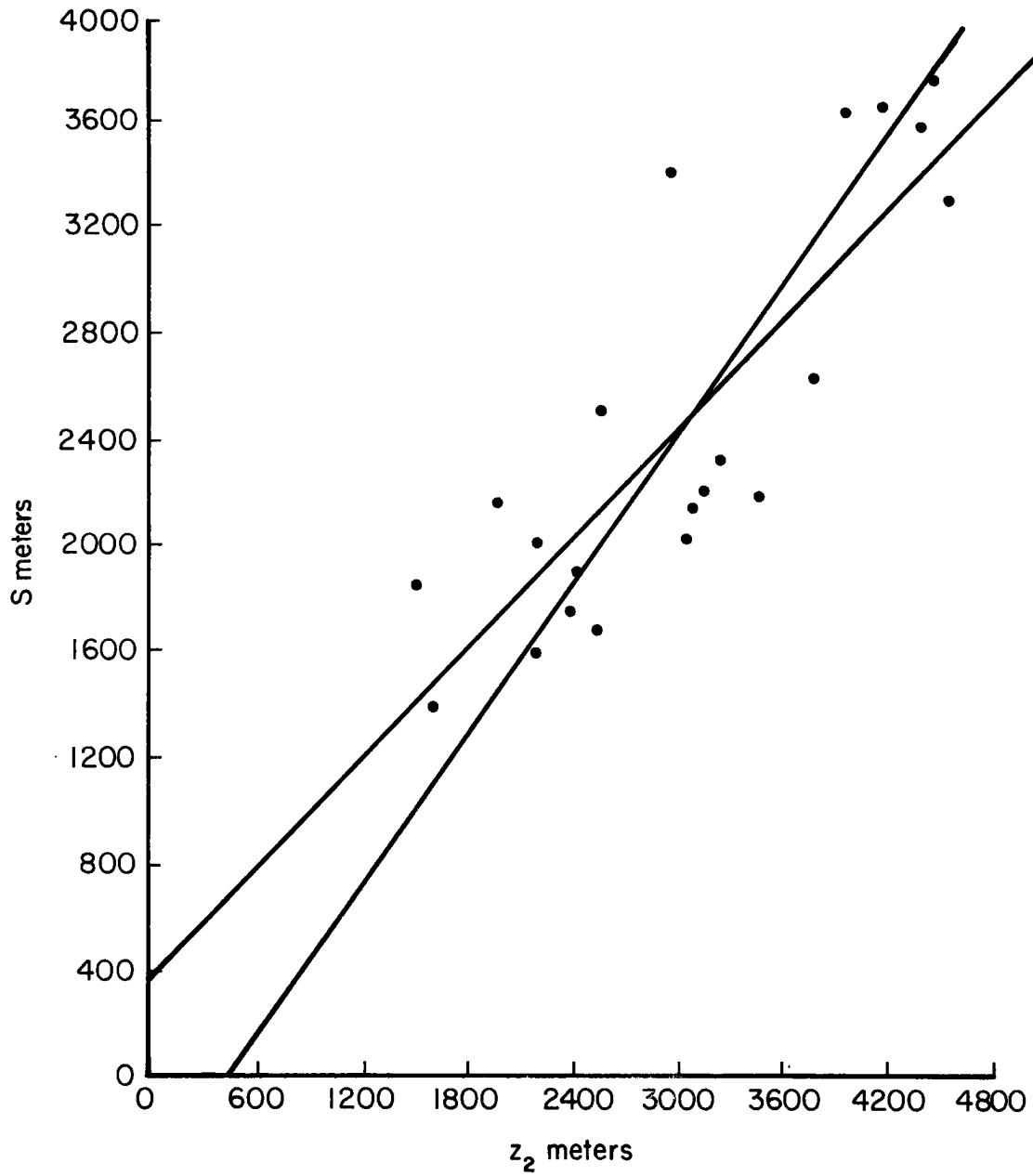


Figure 4.22 - Regression analysis of S onto Z₂. Correlation coefficient of .86.

These formulae are the equations of the lines connecting the origin with the mean values of \bar{S} and the corresponding depths.

The dashed line in Fig. 4.22 represents the functional relationship of S on ΔZ using $\frac{\Delta Z}{a} = 6.5$ (Betts, 1973b) where a is the model cloud tower radius and $\frac{1}{S} = \frac{1}{M} \frac{dM}{dZ} = \frac{9}{32} \frac{K_2}{a}$.

A value of $K_2 = .65$, which agrees well with observational evidence, was used in the calculation (Simpson and Wiggert, 1969).

These values of entrainment also agree with those found by Ruprecht (1971) for small shower clouds.

5. SUMMARY AND CONCLUSIONS

The structure of a set of VIMHEX II sondes, chosen as having a well-defined transition layer, suggests that a substantial portion (about 20%) of the heat flux into the subcloud layer enters from the top of the layer.

The two layer lapse-rate model proposed in Betts (1970, 1973a) was tested for a range of meteorological values applicable to the tropical atmosphere. A necessary and sufficient condition for a solution to exist is that the mean lapse-rate in the cumulus layer ($\bar{\Gamma}$) be more stable than the lapse-rate for an ascending cloud parcel (Γ_c). The thermal structure predicted by the model agreed well with thermal structures observed in BOMEX, ATEX and VIMHEX, although the parameters for entrainment (E) and dissipation of kinetic energy (D) were varied to obtain a best fit. The range of values of E and D required was fairly small, and the mean values (E = 0.45; D = 0.60) also gave close agreement with the observed thermal structure. However, it is likely that vertical wind shear (and other processes) will affect entrainment rate. The comparisons between model and observations did show a relationship between entrainment rate and kinetic energy dissipation ($E + D \sim 1.05$).

It was found that the scaling of entrainment by the depth of the layer of conditional instability (as used in the model) was justified, but that to a similar level of approximation, various other depths of the cumulus layer could be used to scale entrainment.

A few comparisons of model values of E and values derived from radiosonde ascents into cloud indicated general agreement.

REFERENCES

- Arakawa, A. and W. Schubert, 1974: Interaction of a cumulus cloud ensemble with the large-scale environment. Part I. to be published in J. Atmos. Sci.
- Augstein, E., H. Riehl, F. Ostapoff, and V. Wagner, 1973: Mass and energy transports in an undisturbed Atlantic trade-wind flow. Mon. Wea. Rev., 101, pp. 101-111.
- Ball, F. K., 1960: Control of inversion height by surface heating. Quart. J. Roy. Meteor. Soc., 86, pp. 483-494.
- Betts, A. K., 1970: Cumulus convection. unpublished Ph.D. thesis, Imperial College, University of London, 151 pages.
- Betts, A. K., 1973a: Non-precipitating cumulus convection and its parameterization. Quart. J. Roy. Meteor. Soc., 99, pp. 178-196.
- Betts, A. K., 1973b: A relationship between stratification, cloud depth, and permitted cloud radii. J. Appl. Meteor., 12, pp. 890-893.
- Betts, A. K., 1974a: Reply to Deardorff et al. Quart. J. Roy. Meteor. Soc., 100, (to be published).
- Betts, A. K., 1974b: The scientific basis and objectives of the U. S. convection subprogram for GATE. to be published in Bull. Amer. Meteor. Soc. (April)
- Betts, A. K., F. J. Dugan and R. W. Grover, 1974: Residual errors of the VIZ radiosonde hygistor as deduced from observations of subcloud layer structure. Submitted to Bull. Amer. Meteor. Soc.
- Carson, D. J., 1973: The development of a dry inversion-capped convective unstable layer. Quart. J. Roy. Meteor. Soc., 99, pp. 450-467.
- Charney, J. G. and A. Eliasson, 1964: On the growth of the hurricane depression. J. Atmos. Sci., 21, pp. 68-75.
- Deardorff, J. W., G. E. Willis and D. K. Lilly, 1974: Comment on non-precipitating cumulus convection and its parameterization. Quart. J. Roy. Meteor. Soc., 100, pp. 122-123.
- Dugan, F. J., 1973: The thermodynamic structure of the cumulus sub-cloud layer. Atmospheric Science Paper No. 205, Dept. of Atmospheric Science, Colorado State University, 97 pages.
- Gray, W. M., 1972: Cumulus convection and larger-scale circulations, Part III. Atmospheric Science Paper No. 190, Dept. of Atmospheric Science, Colorado State University, 80 pp.
- Holland, J. Z., and E. Rasmusson, 1973: Measurements of the atmospheric mass, energy, and momentum budgets over a 500-kilometer square of tropical ocean. Mon. Wea. Rev., 101, pp. 44-55.

REFERENCES - Continued

- Kuo, H. L., 1963: Perturbations of plane Couette flow in stratified fluid and origin of cloud streets. Phys. Fluids, 6, pp. 195-211.
- Kuo, H. L., 1965: On formation and intensification of tropical cyclones through latent heat release by cumulus convection. J. Atmos. Sci., 22, pp. 40-63.
- Manabe, S., J. Smagorinsky, and R. F. Strickler, 1965: Simulated climatology of a general circulation model with a hydrological cycle. Mon. Wea. Rev., 93, pp. 769-798.
- Ooyama, K., 1964: A dynamical model for the study of tropical cyclone development. Geofisica Internacional Mexico, 4, pp. 187-198.
- Ruprecht, E., 1971: Entrainment as a factor in shower development. Beitrag Phys. Atmos., 44, pp. 1-16.
- Simpson, J., and V. Wiggert, 1969: Models of precipitation cumulus towers. Mon. Wea. Rev., 97, pp. 471-489.
- Stull, R. B., 1973: Inversion rise model based on penetrative convection. J. Atmos. Sci., pp. 1092-1099.
- Steiner, J. T., 1973: A three-dimensional model of cumulus cloud development. J. Atmos. Sci., 30, pp. 414-435.
- Tennekes, H., 1973: A model for the dynamics of the inversion above a convective boundary layer. J. Atmos. Sci., 30, pp. 558-567.

APPENDIX A

Dry Model

The basic equations of the sub-cloud layer model of Betts (1973a) are:

$$\text{Heat budget: } F_{0\theta} - F_{m\theta} = Z_m \bar{\rho} C_p \frac{d\bar{\theta}_d}{dt} \quad (\text{A.1})$$

$$\text{Inversion rise: } F_{m\theta} = - \left(\frac{dZ_m}{dt} - W_m^* - \tilde{W}_m \right) \tilde{\rho}_m C_p \Delta\theta \quad (\text{A.2})$$

where W_m^* is a parameterization for convective mass flux at the top of the mixed layer

$$\text{Closure equation: } F_{m\theta} = -k F_{0\theta} \quad (\text{A.3})$$

and the rate of change of inversion strength

$$\frac{d\Delta\theta}{dt} = \left(\frac{dZ_m}{dt} - W_m^* - \tilde{W}_m \right) \Gamma_1 - \frac{d\bar{\theta}_d}{dt} \quad (\text{A.4})$$

If the left hand side of this equation is neglected in comparison to either term on the right hand side, we obtain by combining A.1 to A.4, a quasi-steady solution for $\Delta\theta$

$$\Delta\theta = \bar{\rho} k \Gamma_1 Z_m / \tilde{\rho}_m (1+k) \quad (\text{A.5})$$

From equations A.3 and A.5 we see that, the inversion strength is directly related to the 'entrainment induced' downward heat flux (see text, Chapter 3) through the parameter k.

Lapse-Rate Model

The non-precipitating cumulus layer is modelled assuming a two-layer structure as discussed in Chapter 4 (Fig. 4.2). The quantities Z_b , Z_2 , $\tilde{\theta}_b$, and $\tilde{\theta}_2$ are assumed known. These define

$$\begin{aligned} \Delta Z &= Z_2 - Z_b = \Delta Z_1 + \Delta Z_2 \\ \bar{\Gamma} \Delta Z &= \theta_2 - \theta_b = \Gamma_1 \Delta Z_1 + \Gamma_2 \Delta Z_2 \end{aligned} \quad (\text{A.6})$$

```
6 ZR = ZR + 0.2
GO TO 10
5 GTWO = GONE/GR
C-----SOLVE K.E. EQUATION
Y = (GCONE - GONE) * DZONE
A = DZTWO * DZTWO
B = - (2.0*Y*DZTWO + D * Y * DZONE)
C = (1.0 - D)*Y*Y
IF (4.0*A*C.GT.B*B) 77, 42
42 QUAD = B*B - 4.0*A*C
DELG = (-B+SQRT(QUAD))/(2.0*A)
C-----NEW GTWO
GTWOP = GCONE + DELG
DELZ = (GCONE - GONE)/(GTWO - GCONE)*DZONE
C-----TEST FOR CONVERGENCE
IF (ABS(GTWOP - GTWO).LT.0.01) GO TO 8
GONEP = GTWOP*GR
C-----NEXT ITERATIVE VALUE FOR GR
GR = GONEP/GTWO
C-----SOLVE CUBIC EQUATION FOR NEW ZR
A = E/(1. - E/2.)
ZR = 1.
J = 1
26 ZRRS = ((A*E)/ZR + A)/GR
J = J + 1
IF (J.GT.20) GO TO 27
```

```
ZRR = SQRT(ZRRS)
IF(ABS(ZRR - ZR).LT.0.0001) GO TO 13
ZR = ZRR
GO TO 26
13 ZR = ZRR
GO TO 10
77 WRITE
   FORMAT (*DELZ IMAGINARY*)
GO TO 8
2 WRITE
   FORMAT (*GCONE IS NOT LESS THAN GBAR*)
C-----WRITE RESULTS
8 WRITE E, D, GONE, GTWO, DZONE, DZTWO, DELZ, ZR
   FORMAT
C-----INCREMENT PARAMETERS
27 E = E + 0.1
   IF (E.GT.0.81) 11, 216
11 D = D - 0.1
   E = 0.2
   IF (D.LT.0.19) 31, 20
25 STOP
END
```